Uncovering the spatial realm of cell metabolism: filament formation of CTP synthase in yeast

Flory A. Olsthoorn

First Examiner: Prof. Dr. Friedrich Förster
Second Examiner: Dr. Tzviya Zeev-Ben-Mordehai
Daily Supervisor: Dr. Stuart C. Howes
17/10/2022

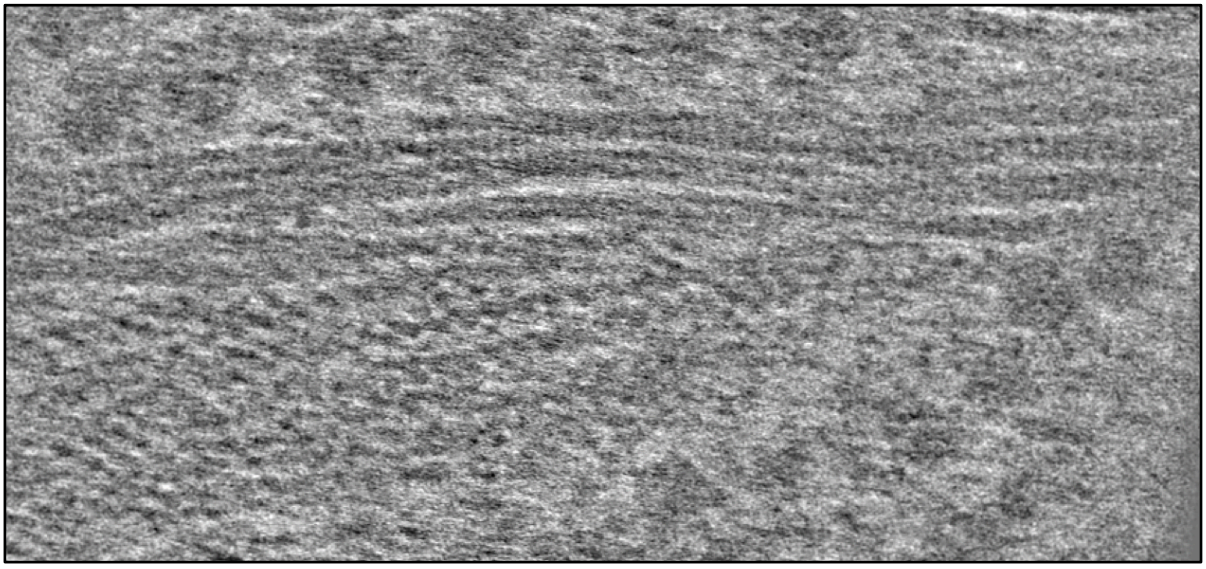

Abstract

Cell metabolism is comprised of a complex network of interactions. Regulating metabolic flux, especially in stress conditions, is essential to cell survival. An increasing number of studies suggest that the spatial organization of metabolic enzymes within the cell plays a critical role in regulating metabolic flux. In *Saccharomyces cerevisiae*, it is speculated that enzyme sequestration is a common mechanism of downregulating product synthesis rates in starvation conditions. Particularly, sequestration by filament formation is reported as a prevalent phenomenon. In this study, we investigate filament formation of CTP synthase *in situ*, using a cryo-CLEM tomography approach. We identify three individual instances of filament bundles and characterize them through filament averaging. To enable efficient implementation of rapid GPU-based template matching for locating CTP synthase in non-filamentous form, we develop a subvolume-based template matching approach. Altogether, we present a methodology that can be adapted for mapping out the spatial organization of metabolic pathways, to improve our understanding of how cells control their metabolism.

Keywords (5): metabolism, cryo-CLEM, CTP synthase, S. cerevisiae, starvation

Layman's Summary

In order for cells to grow, they need energy and building blocks. Certain molecules function as building blocks or carry energy. Enzymes are proteins responsible for shaping molecules to suit their function. Often, for a particular building block to produced, a sequence of different enzymes is needed to obtain the right molecular structure. The process of creating these molecules is called metabolism.

While we know the details of how these metabolic products are formed, how enzymes and their targets interact inside the cell remains to be explored. The cell is a crowded area, with structures and compartments everywhere. For an enzyme to get to its target, it needs to travel there somehow. The crowdedness of the cell serves as a barrier for movement, like trying to move through a crowded station to get to the train.

Metabolic products need to be made in bulk at high speeds for cell growth, so how can a cell ensure maximum production? In this study, we looked at how cells organize metabolic molecules, so the products are created as fast as possible. Additionally, cells should also be capable of slowing down metabolic processes. If an environment lacks nutrients, a cell will stop producing the building blocks needed for growth to save energy. One way of achieving this is through storing enzymes in a shape that makes them inactive, for instance filaments. Filaments are long chains of the same molecule stacked on top of each other. CTP synthase, an enzyme responsible for the production of CTP -a molecule that carries energy- is speculated to form filaments.

Using electron microscopy, we can visualize what these enzymes look like both in free and filamentous form. To target CTP synthase amongst the crowdedness of the cell, a fluorescent tag is attached to the enzyme. We first image a sample of cells with fluorescence light microscopy, and then use electron microscopy. By overlaying the fluorescent images with the electron images, we can find our area of interest. A series of images is taken at that spot with the electron microscope while tilting the sample along an axis. The obtained images can subsequently be combined to create a 3D image of the area.

In our research we find three bundles of filaments near the area of our fluorescence. We suggest these filaments are made up of CTP synthase. Unfortunately, we need to acquire more and higher quality data before we can conclude this. However, the method we developed to obtain these images of filament bundles can be applied to study many different metabolic pathways inside cells. A combination of electron and fluorescence microscopy is key to uncovering how enzyme and substrate interact inside the cell. This will aid our understanding of how a cell grows and adjusts to its environment.

Introduction

Diffusion-based motion cannot account for metabolic synthesis rates

Cell metabolism is a highly complex and coordinated system of interactions, responsible for supplying the cell with energy and synthesizing new essential molecules. The function and growth of a cell depends on its metabolism. Therefore, it is crucial that the activity of the enzymes involved is optimized. Regulating enzyme abundance through altering transcription or translation rates is one way of adjusting metabolic flux. Post-translational modifications that alter the catalytic properties of metabolic enzymes have also proven to be essential, predominantly because of their rapid and immediate influence on the metabolic product synthesis rate **[Wang et al., 2010; Krebs et al., 1979]**. In addition to these general mechanisms of regulation that directly affect enzyme abundance or activity, studies suggest that cells also manage their metabolism on a spatial level through protein accessibility **[Gaertner, 1978; Sweetlove et al., 2018]**.

While the optimal performance of metabolic pathways in the spatial dimension was previously assumed to be the result of a "well-mixed" system, ongoing research challenges this classical perception **[Schmitt et al., 2017]**. In a rudimentary model, the cytosol of a cell is equated to a homogeneous, aqueous solution through which molecules can freely diffuse. The spread of metabolic enzymes, cofactors, and intermediates is thus based on Brownian motion **[Barros et al., 2007]**. However, if such a model is applied to experimental data, the resulting diffusion factors diverge considerably **[Selivanov et al., 2007]**. Besides, the observed synthesis rates are higher than allowed by free diffusion of reactants or products **[Saks et al., 2008]**. Cellular structural elements such as internal organelles, cytoskeletal networks, and macromolecular crowding function as local diffusion barriers and limit the actual diffusion rate of molecules inside the cell **[Saks et al., 2008]**. Hence, it can be concluded that the cytosolic compartment of the cell is not in fact a homogeneous system. A "well-mixed" system is only theoretically possible and does not serve to spatially maximize nor regulate metabolism. Although the spatial dynamics and compartmentalization of metabolic enzymes have been observed for decades **[McBrien et al., 1968]**, only recently has the role of these phenomena in regulation of metabolism come to light. Reevaluation of the classical understanding of how metabolic pathways spatially optimize to adjust their production rates is in order (Figure 1A).

Multienzyme complexes as reaction hubs for metabolic pathways

Historically, existence of complex structural organization -also known as "quinary structure"- has been studied in cell-free systems **[Cohen et al., 2017]**. Multienzyme complexes are hypothesized to function as "membraneless" compartments containing key agents of a metabolic pathway. These compartments serve as reaction hubs for the chemical interactions necessary. By confining the essential molecules of a pathway within such a space or complex, substrate channeling is facilitated and reaction rates are maximized **[Castellana et al., 2014; Bauler et al., 2010]**. Additionally, potential toxic or unstable precursors can immediately be processed through proximity to successive enzymes and cofactors. Colocalization of metabolic enzymes and their structural interaction is therefore considered paramount to regulation of metabolic flux.

Not only can metabolism be regulated through multienzyme complexes that increase overall reaction rates; enzyme sequestration also plays a critical role by decreasing product synthesis rates [Hinzpeter et al., 2019]. Especially while exposed to environmental stress, cells often rely on downregulation of their cellular metabolism as a major response strategy [Hand & Hardewig, 1996]. In case of nutrient deficiency, restricting metabolic synthesis is an effective way of saving energy and resources. Sequestration of enzymes can create a spatial barrier that reduces the activity of the enzyme in question without necessarily altering its catalytic properties or disposing of the protein. Thus, achieving sequestration should not be a costly process and it allows the cell to quickly recover when conditions reverse. In fact, self-assembly of metabolic enzymes into filaments appears to be a widespread phenomenon, particularly at the rate-limiting step of metabolic pathways [Noree et al., 2019; Lynch et al., 2020; Park & Horton, 2019; Simonet et al., 2020]. As a review on the topic by Schmitt et al. proposes; metabolic flux is regulated by alternating states of multienzyme assembly and sequestration (Figure 1B) [Schmitt & An, 2017].

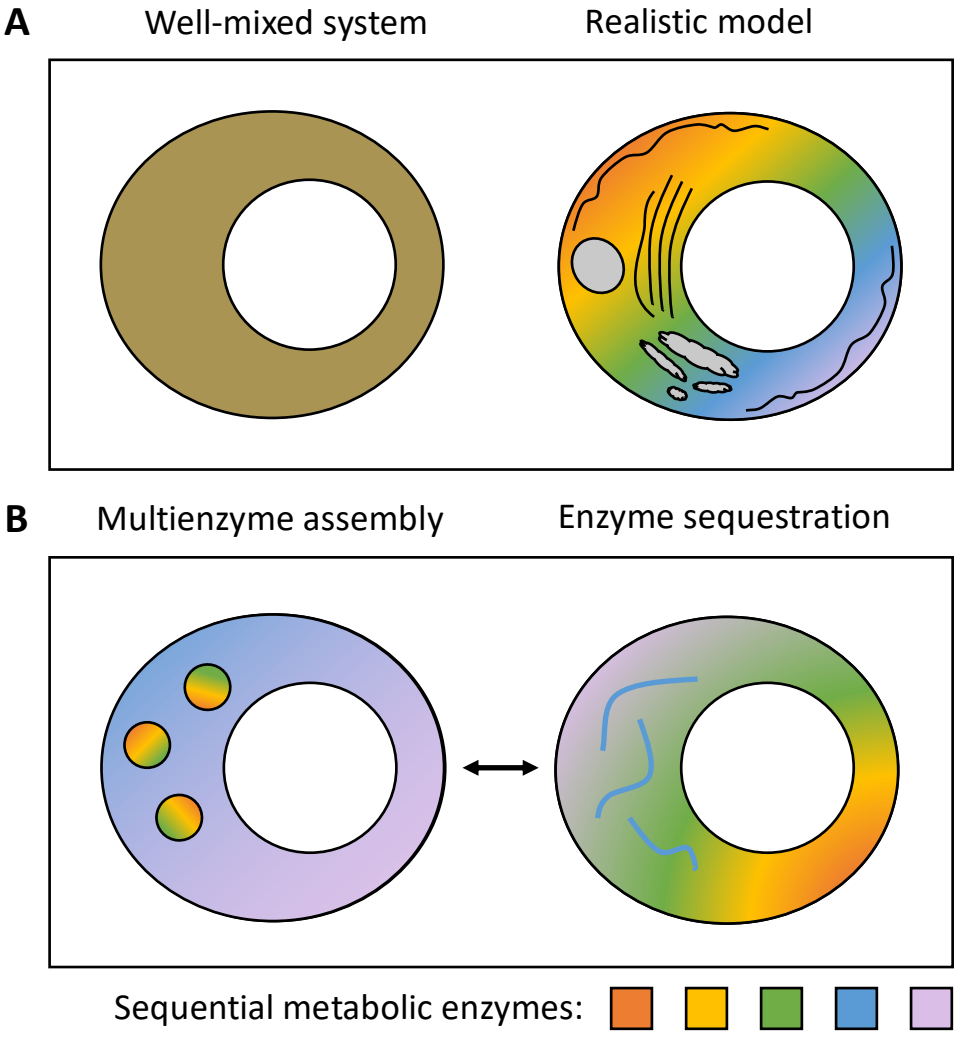

Figure 1: Regulation of metabolic flux through spatial optimization.

(A) A spatially well-mixed system by diffusion is unattainable in a realistic setting. It cannot not account for the local diffusion barriers presented by the cytoskeletal network, intracellular organelles, and macromolecular crowding. (B) Within a realistic model, enzymes form multienzyme assemblies to maximize product synthesis. In response to environmental stress, cells can stall metabolism through sequestration of essential enzymes.

A robust method for structurally characterizing spatial organization in native context is needed

Most of our current knowledge on the existence of multienzyme assembly and enzyme sequestration comes from in cell studies. A variety of light microscopy techniques are employed to investigate spatial organization phenomena **[Schmitt & An, 2017]**. From glycolysis and gluconeogenesis enzymes clustering to formation of the fatty acid synthase complex in fatty acid synthesis; most of the essential metabolic pathways seem to be spatially optimized in some manner **[Kohnhorst et al., 2017; Suresh et al., 2015; Gipson et al., 2010; Noree et al., 2019]**. Even nucleotide synthesis is regulated through polymerization and dynamic cellular bodies, called "purinosomes" **[Liu, 2016; French et al., 2016]**. However, actual structural information on the interaction mechanisms and the consequences of these phenomena is still lacking. If such information is available, it is usually derived from *in vitro* studies or an overexpressed state of the protein **[Marini et al., 2020]**. In order to determine the functional significance of these spatial assemblies in a cellular context, we require structural characterization of the processes involved. For development of a method that can attain this kind of information, CTP synthesis in yeast serves as an ideal model metabolic pathway. Filament formation of CTP synthase (CTPS) has been structurally and biochemically characterized in depth **[Hansen et al., 2021; Ingerson-Mahar et al., 2010]**. Its assembly mechanism, however, is yet to be explored in a native state.

We aim to map out the spatial organization of de novo CTP synthesis in *Saccharomyces cerevisiae* at molecular resolution, while obtaining structural information on CTPS accumulation. By determining the structure of CTPS in a sequestrated state in cell, we can elucidate the mechanism by which the cell regulates its CTP synthesis rate. As CTPS accumulation within foci is a response to starvation stress, this research will give insight into how yeast manages pyrimidine metabolism in conditions where growth is undesirable **[Noree et al., 2010]**. As Noree et al. observes, many other metabolic enzymes in yeast accumulate under starvation conditions **[Noree et al., 2010]**. Therefore, whether CTPS forms filaments in cells will shed light on the comprehensive metabolic stress response in yeast. Moreover, the methodology developed in this study can be adapted for analyzing the spatial organization of metabolic enzymes in general. This research may contribute to uncovering the spatial dimension of metabolism within its cellular milieu.

Results

GFP-tagged Ura7 assembles into foci upon starvation

Cytidine triphosphate synthase (CTPS) interconverts CTP and UTP in de novo pyrimidine biosynthesis. This reaction comprises the final step of the CTP synthesis pathway and is also the rate-limiting reaction **[Lieberman, 1956]** (Figure S1). Across the many domains of life, CTPS has been observed to assemble into filaments: polymeric structures with CTPS as the repeating unit **[Zhou et al., 2021; Noree et al., 2010; Ingerson-Mahar et al., 2010; Barry et al., 2014]**. CTPS has two isoforms in budding yeast: Ura7 and Ura8. The molecular concentration of Ura7 inside the cell is tenfold that of Ura8 **[Nadkarni et al., 1995; Ghaemmaghami et al., 2003]**. This study will focus on Ura7 CTPS sequestration because its abundance facilitates accurate targeting and analysis. Ura7 is active in a tetrameric state with a total mass of approximately 260 kDa **[Yang et al., 1994]**. The enzyme responsible for catalyzing the first two steps of de novo pyrimidine biosynthesis is Ura2, which has not been reported to engage in enzyme sequestration **[Antonelli et al., 1998; Noree et al., 2019]**.

As Hansen et al. demonstrates, isolated Ura7 polymerizes in tetrameric form into parallel filaments. At lower pH, larger bundles of filaments emerged as a result of lateral aggregation of singular filaments **[Hansen et al., 2021]**. These filament bundles are in accordance with live cell fluorescent light microscopy (FLM) experiments that primarily show one focus of signal accumulation per starved cell. Hansen et al. even observed the initial appearance of multiple small foci that later converged into one larger signal, resembling *in vitro* behavior **[Hansen et al., 2021]**. Although numerous studies have shown accumulation of fluorescently tagged CTPS in starved cells, whether this accumulation constitutes filament formation has yet to be explored.

To establish a protocol for inducing Ura7 accumulation in yeast, an FLM experiment described in previous studies was reproduced **[Hansen et al., 2021, Noree et al., 2010]**. Yeast cells with endogenously GFP-tagged Ura2 or Ura7 were harvested while in log phase and incubated in starvation medium. The GFP-signal of the target proteins appeared outside the vacuoles and nucleus, as was expected due to the largely cytosolic nature of both proteins. The nucleus was not distinguishable from the vacuoles with certainty. In log phase, the general dispersion of both Ura2 and Ura7 appeared homogeneous throughout the cytosol at this resolution (Figure 2A). Upon nutrient deprivation, Ura7 accumulated to form bright foci, whereas the distribution of Ura2 remained uniform (Figure 2A).

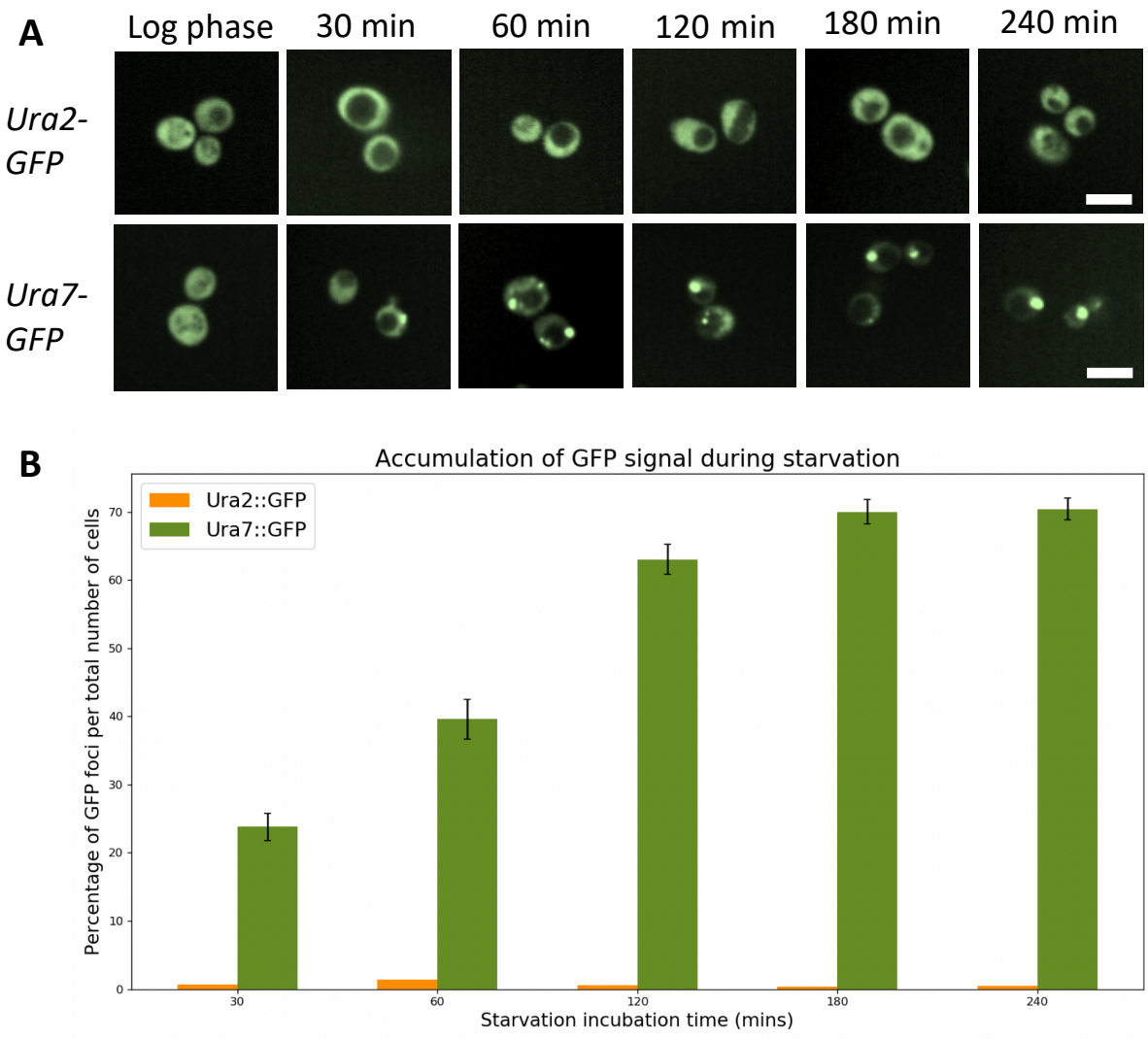

Figure 2: Signal accumulation of CTPS in response to starvation stress.

(A) The spread of Ura2 and Ura7 throughout the cytosol is largely even in a log phase state of growth of the cell. Upon starvation stress, Ura7 accumulates into foci. Cells were incubated in starvation medium for varying amounts of time. Ura2 dispersion was barely affected. Accumulation of Ura7 increased over time. The percentage of foci per total number of cells was quantified per condition. Scale bar: 5 μm. (B) The calculated percentage of foci was plotted for each timepoint. The error bars represent a binomial 95% confidence interval.

The experiment was performed for different starvation timepoints to determine the incubation time necessary for inducing the maximum number of filaments (Figure 2A). Quantification of both Ura2 and Ura7 fluorescence data allowed for a fair comparison (Table S1, Figure 2B). After 30 minutes of incubation, Ura7 puncta were already observed. The total number of cells counted for this condition amounted to 1,766. The total number of foci counted was 421. As the number of foci per individual cell could not be efficiently determined, the measure used to quantify the increase in foci equaled the total number of foci per total number of cells and thus corresponded to 24%. Furthermore, some cytoplasmic areas of the cells not exhibiting distinct points of fluorescence started losing or gaining signal compared to the control condition. Unfortunately, at this resolution, no quantifications of the

change in brightness of GFP-signal could be made. However, as time increased, foci did visually seem to become brighter and sometimes larger. After 1 hour, the number of foci had effectively doubled, corresponding to 40%. From 1 to 2 hours, a steady increase was again perceived to 63% foci, while the surge in fluorescent maxima slowed after 2 hours. Between 3 and 4 hours, the rise in signal accumulation plateaued at 70% (Figure 2B). Most cells with putative filament formation presented more than one focus per cell prior to reaching 2 hours of starvation. Remarkably, while the total number of cells forming foci increased, the number of foci per individual cell often appeared to decrease from multiple fluorescent spots to one after 2 hours.

In contrast to the rapid rearrangement of Ura7, there were no obvious foci detected for Ura2, nor was there a surge in signal accumulation over time. After 4 hours of starvation, the distribution of the GFP-signal had rearranged to a limited extent, with some areas of the cytoplasm exhibiting brighter fluorescence. Generally, the fluorescence of Ura2-GFP expressing cells after 4 hours seemed to have dimmed. Thus, Ura7 accumulates into singular spots in the cytoplasm as a result of nutrient deprivation, while the dispersion of Ura2 throughout the cell stays diffuse.

Protein expression levels are predominantly unchanged by starvation

To assess the influence of starvation on the yeast protein landscape, a selection of proteins was studied through Western blot analysis. Determination of the lysate protein concentration showed that the total amount of protein expression did not change drastically upon starvation (Figure S2). Instead, concentrations were stable, amounting to approximately 1 μg/μL for all samples (Table S2/S3).

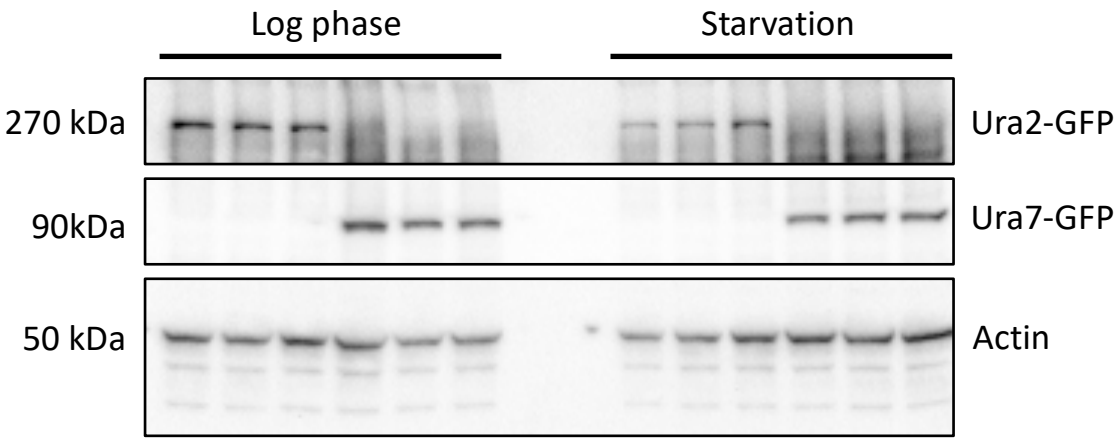

Figure 3: Protein concentration of yeast lysates seems unchanged upon starvation.

A Western blot was performed with the lysates measured in Figure S2A. Protein expression levels of Ura2 and Ura7 were mostly unaffected by starvation stress.

Protein abundance of Ura7 remained largely constant as band intensity did not change substantially between states of growth and starvation (Figure 3). For Ura2 expression, a decrease in signal intensity upon nutrient depletion was observed. The loading control, actin, showed a corresponding

drop in signal. Likely, Ura2 expression was stable across the different growth conditions and the detected reduced signal is a product of less sample loaded overall. A replicate of the analysis resulted in a similar overall outcome, as the intensity of the target proteins stayed consistent for both conditions in the second blot (Figure S3). Equally, the loading control displayed homogeneous intensity throughout the different lanes. Thus, total protein determination of lysates shows that the overall protein abundance in yeast is not strongly affected by starvation. Specifically, Western blot analysis shows that Ura2 and Ura7 protein abundance is comparatively uninfluenced by absence of nutrients.

Identification and characterization of potential Ura7 filament bundles *in situ*

To achieve high resolution structural information of native protein states, cryo-electron tomography (cryo-ET) was implemented. As sample thickness is a limiting factor for cryo-ET, focused ion beam-milling (FIB-milling) was used to thin vitrified samples prior to data collection. FLM under cryogenic conditions allowed for navigating the sample and identification of the sites of interest. Employing a cryo-correlative light electron microscopy (cryo-CLEM) approach, fluorescently tagged CTPS was targeted during FIB-milling and data collection. The fluorescent signal also served as a confirmation tool once filament structures had been identified.

Using this specifically designed cryo-CLEM tomography pipeline, the assembly of the Ura7 fluorescent signal was studied *in situ* (Figure 7). Tilt series were recorded at the sites of correlated fluorescent signal (see Methods). Ultimately, after visual inspection of the resulting reconstructed volumes, a structure resembling the morphology of the ordered filament bundles characterized by Hansen et al. *in vitro* was identified (Figure 4A) **[Hansen et al., 2021]**. The filament bundles stretched the length of approximately 500 nm, with a bundle width of 150 nm. As cryo-samples were thinned to allow for tomographic data collection, the size estimates might be limited. However, the density of the bundle appeared to round off at the edges, indicating that most of the original volume of the structure was present in the tomogram. The bundle seemed compromised of roughly 8 nm thick filaments. Amongst the filaments, two different types of repeating unit were discerned: one of circa 5 nm, the other of 8 nm (Figure 4A). However, the filaments exhibiting the smaller repeat did appear to extend into the area projecting the larger repeating unit (Figure 4A).

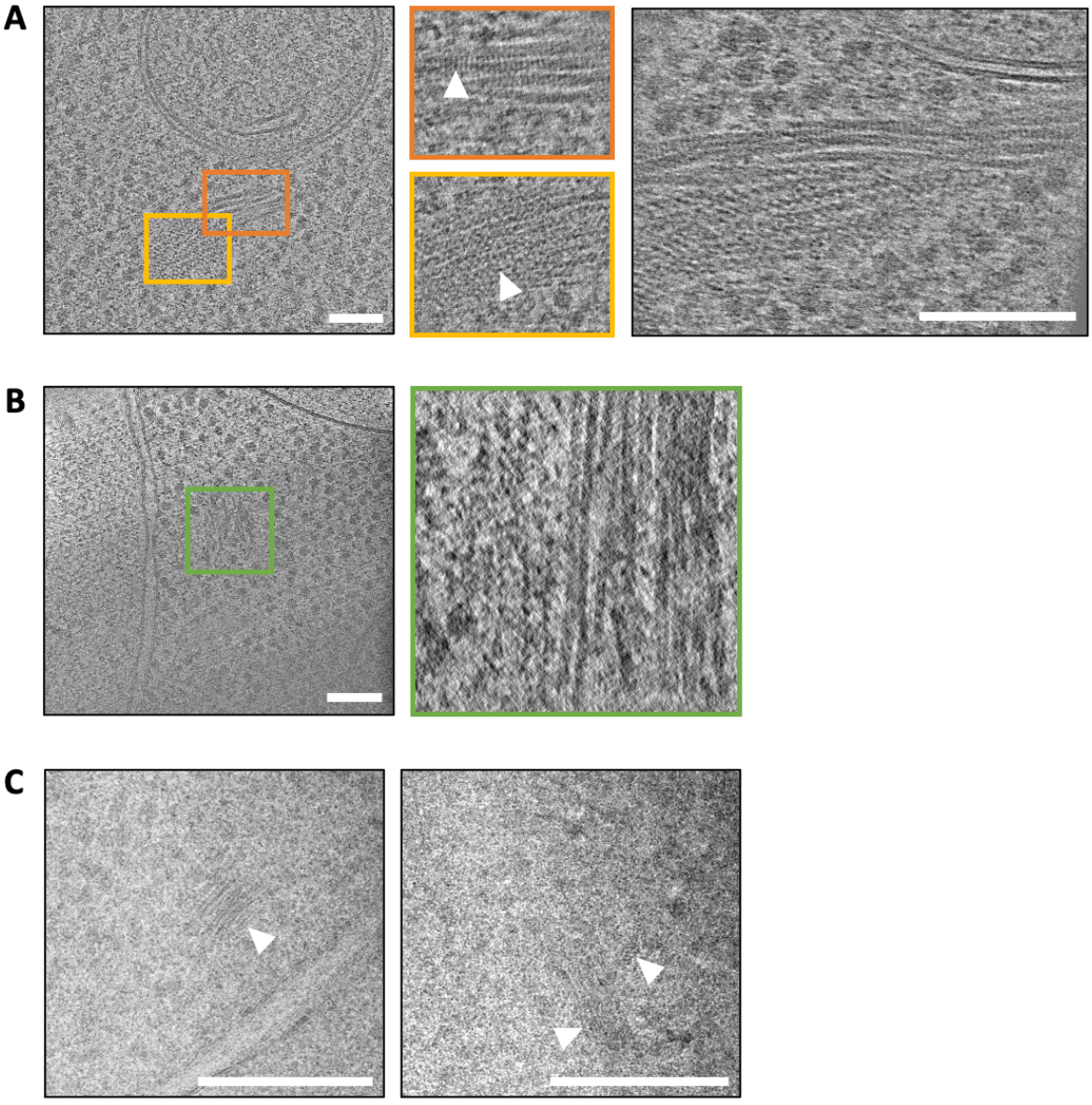

Figure 4: A cryo-CLEM approach successfully localizes filament densities at the sites of Ura7 signal.

(A) The identified filament structure is comprised of bundled filaments. Two different types of repeating unit are observed, as shown by the white arrows. Scale bar: 100 nm. (B) Another filament bundle was discovered. The observed filaments resemble those found in A. Scale bar: 100 nm (C) A third filamentous bundle was localized. High dose images were taken. The white arrows point to the filament density as well as the occurrence of the repeating unit in the image on the right. Scale bar: 200 nm.

Another tomogram unveiled a filament bundle with similar morphology (Figure 4B). Here, only the larger repeating unit was observed, although filament shape was reminiscent of the assembly exhibiting the smaller repeat. Finally, a third filament bundle was located at another GFP-signal site (Figure 4C). A tilt series could not be collected, but a high-dose image showed a bundle that bore most semblance to the structure as seen in the second tomogram. Again, the larger repeat was observed.

For initial characterization of the different repeating units, power spectra were computed (Figure 5A). The power spectrum of the 5 nm repeat revealed a distinct punctum, indicating a similar orientation for all sampled particles. The power spectrum of the 8 nm repeat instead displayed a pattern resembling a line, possibly suggesting a helical twist along the filament axis. However, the weakness of the signal significantly limits the reliability of any structural deductions.

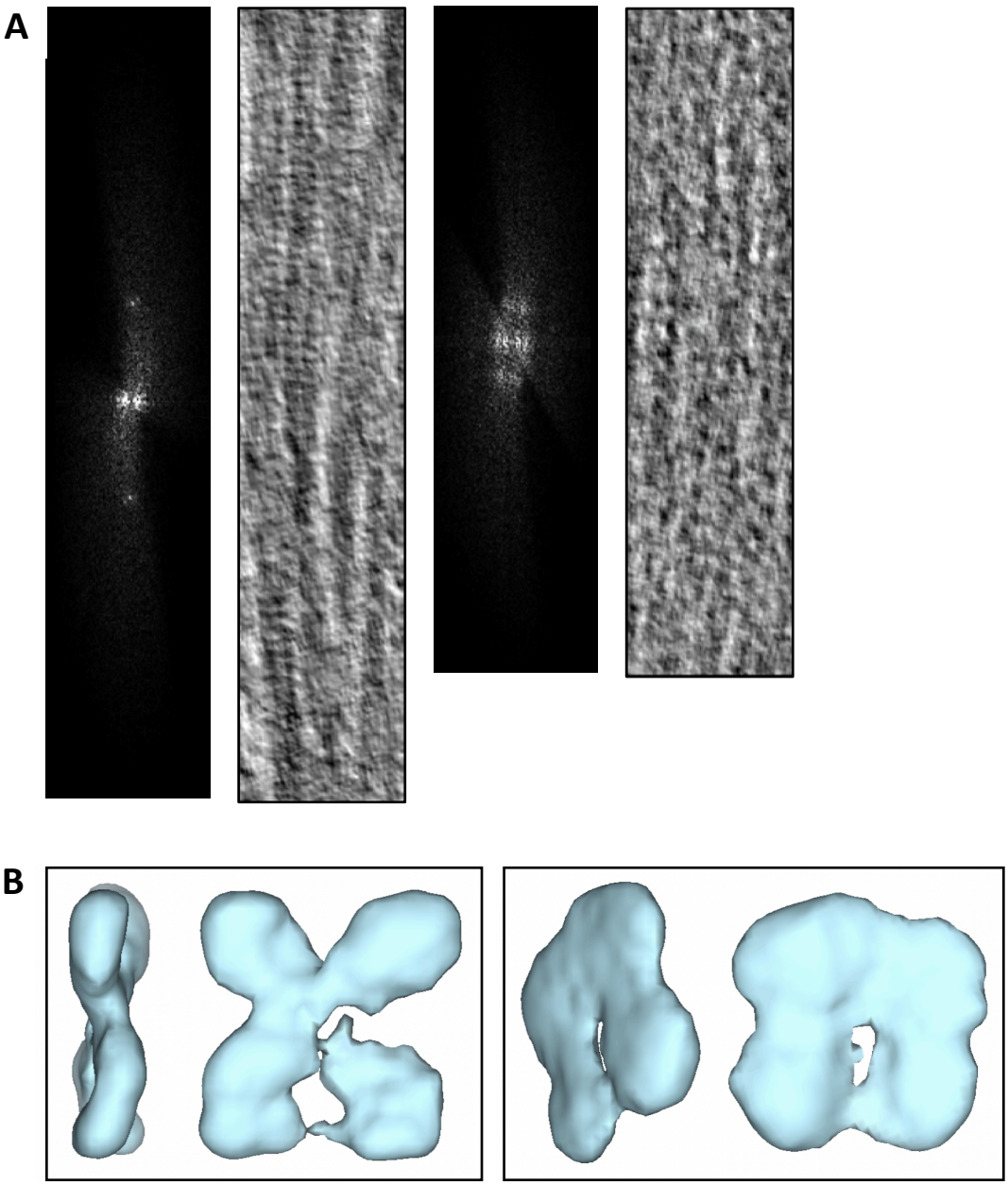

Figure 5: Analysis of the repeating units followed by subtomogram averaging.

(A) The power spectra retrieved for the 5 nm repeat (left) and the 8 nm repeat (right). (B) The averages obtained from run039 and run041 respectively. Run039 was performed using both a reference and a mask, run041 utilized only a mask. The averages were filtered according to their determined resolution of roughly 15 Å.

To uncover the filament structure and determine the origin of the different repeating units, filament averaging was performed (Figure 5B, Table S5). Approximately 2100 particles were picked with a particle size of approximately 4 nm. Introducing the Ura7 filament structure of Hansen et al. as a reference in addition to a cylindrical mask, the average appeared almost identical to the expected Ura7 structure, spanning around 8 by 8 nm (Figure 5B, Figure S4C) **[Hansen et al., 2021]**. When averaging with a randomly assigned particle as reference, a similarly sized density occurred. However, this density lacked the clear definition of the four monomers of the Ura7 tetramer. Instead, a flatter structure was shown, representing a square with some missing density in the centre. To conclude, we show the successful acquisition of tomographic data on filamentous densities corresponding with Ura7-GFP signal. The features of the structural average obtained without a given reference could potentially represent the dimensions of the expected tetrameric Ura7 structure, although the data is not conclusive.

Subvolume-based template matching enables use of GPUs

A subtomogram averaging workflow was established for locating and characterizing Ura2 as well as Ura7 in a non-filamentous state. GPU-based template matching was considered a desirable particle picking method due to its efficiency, but it was limited by the available GPU memory. A memory limitation is overcome either by binning the volume used for template matching, or by splitting the volume up into subvolumes. Considering that the molecular weight of both proteins in active form corresponds to roughly 250 kDa, particle picking in a highly-binned volume would not be favourable. Instead, we designed a subvolume-based template matching approach using PyTom.

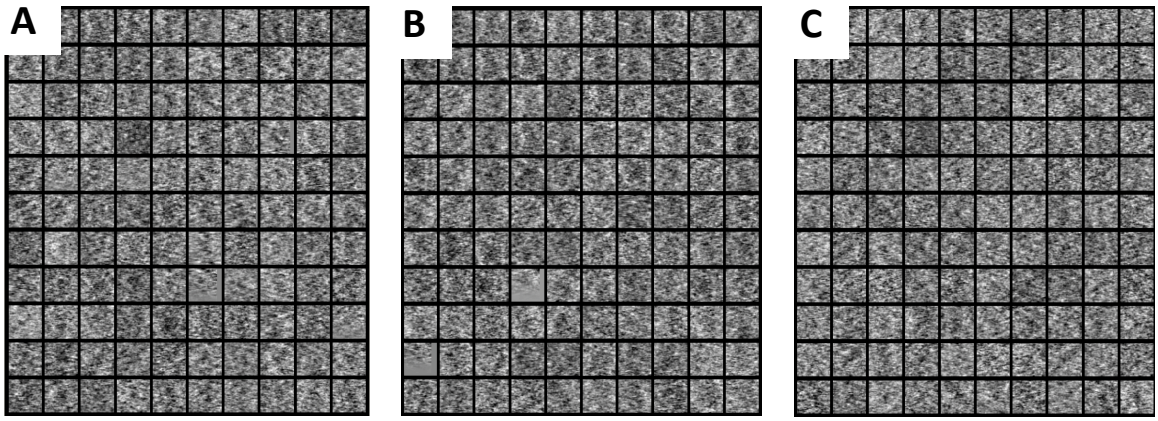

Figure 6: The transformation of the subvolume-based template matching approach was successful.

The particle lists show a 2D pixelated slice of each selected particle. (A) Particle picks of a template matching job ran with a ribosome as reference. (B) Particle picks of a template matching job ran with polymerase gamma as reference. (C) Particle pickso of a template matching job ran with Ura2 as reference.

Subvolumes were created to encapsulate separate parts of a tomogram. Template matching was performed using GPUs. The jobs were consecutively submitted to the GPU with GNU parallel – a tool developed for executing shell jobs in parallel, allowing for an efficient execution **[Tange, 2011]**. After obtaining the particle picking results, particles were extracted. Before continuing with the standard

STA procedure, the identified particle coordinates were transformed and plotted back into the full tomogram, as PyTom subtomogram reconstruction utilizes the original projections of the tomogram. Simultaneously, the particle filenames were rewritten to avoid overwriting during generation of the subtomograms. To test whether the creation of the subvolumes as well as the associated transformation of the particle coordinates was successful, a positive control was implemented using a ribosome as a reference. The resulting particle list clearly displayed centered ribosome densities (Figure 6A). A negative control was used to get an impression of the performance of the template matching algorithm on small proteins. This negative control comprised polymerase gamma as a reference, which is a mitochondrial polymerase of similar mass and size to Ura2. For the number of particles that were extracted, all seemed to correspond to ribosome densities (Figure 6B). Finally, template matching was performed with Ura2 as a reference. The resulting particles looked comparatively similar to each other and did not obviously resemble ribosomes (Figure 6C). To conclude, a pipeline for subvolume-based template matching was successfully developed, although the performance of the resulting method has yet to be examined.

Discussion

Maintenance and adaptation of metabolism during starvation is essential for cell survival. The intracellular compartmentalization of CTP synthase plays a critical role in balancing pyrimidine biosynthesis across many species **[Ingerson-Mahar et al., 2010; Liu, 2010; Carcamo et al., 2011].** In this study, we set out to establish a methodology for mapping out the spatial organization of metabolic pathways on a molecular level. Using *de novo* CTP synthesis as a model metabolic pathway, a cryo-CLEM pipeline was developed to structurally characterize physical organization of metabolic enzymes *in situ*.

Filament induction of Ura7 is a pH-sensitive reaction to starvation

As was established in both Hansen et al. and Noree et al., endogenously GFP-tagged CTP synthase accumulates in yeast cells upon nutrient deprivation **[Hansen et al., 2021; Noree et al., 2010]**. Furthermore, Hansen et al. showed that the formation of CTP synthase filaments is pH-dependent *in vitro* **[Hansen et al., 2021]**. Previous studies have shown that starvation conditions induce cytoplasmic acidification in yeast, triggering macromolecular crowding **[Munder et al., 2016]**. The resulting strongly reduced diffusional mobility within the cell is responsible for a global decrease in metabolic activity and growth **[Joyner et al., 2016]**. Acidification of the cytosol seems to be the assembly trigger for CTPS and other similarly aggregating enzymes to preserve the cell in a low-nutrient milieu. Sequestration of these enzymes in starvation conditions is advantageous compared to disposal, as it is less costly, and allows the cell to store enzymes only to rapidly recover once the environment regains a favorable concentration of nutrients.

Therefore, it is likely that Ura7 accumulation is a direct starvation response, meant to reduce metabolic activity. Ura7 is possibly inactivated through aggregation, as the Ura7 filaments observed by Hansen et al. stabilize an inactive conformation of the protein **[Hansen et al., 2021]**. At a minimum, CTP synthase activity is reduced due to inaccessibility of the active sites within the filament bundles. Additionally, filaments may serve as diffusion barriers that limit the motion of metabolites through the cytosol, slowing down growth processes in general **[Petrovska et al., 2014]**. Filamentous assembly of metabolic enzymes in response to starvation is speculated to be a common mechanism of inhibition in yeast **[Petrovska et al., 2014]**. In fact, metabolic enzymes in general are often found to self-assemble into larger structures, into both activating and deactivating states **[O'Connell et al., 2012]**. In addition to Ura7 foci formation, we showed that Ura2 dispersion throughout the cytosol did not significantly change even under extreme starvation conditions (Figure 2). This observation supports a model in which yeast regulates CTP synthesis by managing the rate-limiting step of the pathway, whereas the enzymatic steps performed by Ura2 are not spatially hindered.

CTP synthesis is regulated through spatial organization of the rate-limiting step

Generally, the overall protein concentration of yeast lysate was not affected by starvation. Either the ratio of protein expression levels changes in response to starvation, or cells regulate their metabolic flux without adjusting protein abundance significantly. Post-translational modifications could play a

role in the inactivation of metabolic proteins during starvation. On a larger scale, we consider the physical organization of the cell. From the fluorescence studies performed, it was concluded that yeast does not necessarily spatially organize Ura2. Additionally, the protein expression levels of Ura2 or Ura7 are not drastically minimised upon starvation. This indicates that Ura2 activity is not strongly regulated through alteration of enzyme abundance or activity, which supports the model previously proposed in which only the rate-limiting step of a reaction is responsible for regulation of metabolic flux. Multiple studies on the regulation of metabolic pathways have shown that the rate-limiting step is often the enzymatic reaction that is sequestered **[Noree et al., 2019; Saad et al., 2017; Jin et al., 2017]**. As we have not measured the synthesis rates of CTP inside the cell with and without CTPS filaments, we can only speculate that the spatial organization of the rate limiting step is responsible for limiting the product synthesis rate of the CTP synthesis pathway. It seems the inherent activity of Ura2 is unaffected by the growth state of the cell.

Prospective insights on the cryo-CLEM approach for targeting filaments

Using the cryo-CLEM workflow developed for targeted FIB-milling and cryo-ET data collection, filament bundles were observed near the site of Ura7-GFP signal in three isolated instances. Unfortunately, the following limitations restricted the throughput of this method even more than is typical for cryo-EM studies.

Firstly, cryo-FLM data are acquired before sample thinning is executed. As a result, much of the fluorescent signal recorded before FIB-milling corresponds to material no longer present in the thinned sample. Equipping the Aquilos Cryo-FIB instrument with an integrated cryo-FLM module such as the Delmic METEOR would enable the collection of fluorescence data when the sample is close to its final thickness. This would help minimizing both polishing and cryo-TEM time spent on lamellae that do not contain the target of interest. Alternatively, lamellae could be transferred to a cryo-FLM microscope between fine milling and polishing of the sample.

Furthermore, the correlation procedure used for aligning FLM data with TEM overviews is not entirely robust. The alignment of SEM images with the corresponding FLM data is performed based on the correlation of the Dynabeads. The Dynabeads are picked in both SEM and FLM data, resulting in reliable scaling and transformation factors to be used for alignment. Any other alignment hereafter, however, is currently performed by eye. The manual correlation mostly relies on lamella shape, cell edges, or other relatively large features. Instead, the scaling factor between FLM and TEM data could be calculated based on the pixel size. This would at least ensure accurate scaling of the FLM image to the TEM overview. An ImageJ plug-in such as DS4H Image Alignment could perform reliable translation and rotation of the fluorescent maximum intensity projection (MIP) and SEM images based on manually picked landmarks in a fashion similar to the selection of the Dynabeads (https://github.com/illeb/DS4H-Image-Alignment), in turn enabling more accurate FLM to TEM correlation. Options such as these would significantly improve the reliability of the method. The use of intracellular beads could also pose as a solution, but their introduction into the cells might prove complicated in this context.

Besides a limited resolution and an error-prone correlation method, the throughput of this approach is further limited by the resolution of the FLM data. Resolution is limited because immersion

objectives cannot be used for cryo-imaging. Due to the limited resolution of the fluorescent signal, determining an exact target for tilt series collection is difficult. Usually, collection of EM images of the site of interest was required beforehand. This additional exposure to electrons reduces the quality of the tilt series acquired. Instead, this workflow would benefit from the incorporation of cryo-superresolution techniques. Alternatively, post-acquisition refinement of the FLM data could possibly be implemented by training and using a neural network such as CARE **[Weigert et al., 2018]**. Altogether, the throughput of the developed cryo-CLEM methodology is mainly limited by the current approach to acquiring and processing the FLM data. A reliable correlation procedure would serve as an immediate improvement, whereas refinement of other factors requires stronger intervention.

The molecular identity of the filament repeats remains unknown

The methodology developed in this study resulted in the localization of three filament bundles near the site of Ura7-GFP signal. All structures resembled each other, as well as the structure observed *in vitro* by Hansen et al., which leads us to believe that these filaments are made up of Ura7 molecules **[Hansen et al., 2021]**. In tetrameric form, Ura7 stretches approximately 8 nm in both width and length. The measured thickness of the filaments is consistent with these dimensions. Two different repeating units were observed along the filament bundles. Power spectra were retrieved to give insight into the molecular conformation of these seemingly different filamentous structures. Since the larger repeat exhibits a helical twist, whereas the smaller repeat represents a stacking conformation, the difference in repeating units could be related to a different polymerization assembly of the same molecule. Possibly, filaments are more dynamic in a cellular milieu than in an isolated state *in vitro*. Equally, the filaments could be built from different molecules altogether, or longitudinal elongation of the polymer could affect the structure. Regardless, it remains difficult to decide whether the filaments themselves are truly comprised of Ura7 without further processing.

One of the filament bundles was characterized through averaging, providing further insights into the molecular building stones. Unfortunately, the particle size chosen for picking and processing of the particles proved unsatisfactory: an approximate interval of 4 nm was used whereas the observed repeating units were either 5 or 8 nm in size. The same applies to the boxsize. Moreover, the different repeating units were part of the same model and therefore not analysed separately. Instead, to decide whether the observed difference in repeating unit is a projection artefact or the result of an actual structural variety, two models will need to be picked. Particles should be extracted with either a 5 or 8 nm interval, corresponding to the two different repeats observed. Furthermore, the boxsize should be increased to encompass at least three molecules, allowing for better alignment as well as obtaining information on the interaction interface. Although the dimensions of the average acquired represent the larger repeat and a tetrameric conformation of Ura7, the resolution of the structure is limited by the inclusion of the smaller repeat. Additionally, the approximate 4 nm interval used to pick particles means that the density of a molecule in the filament is oversampled and most likely not centered.

We conclude that a revision of the filament averaging is necessary, to characterise the two repeating units. Also, more data collection of filament bundles corresponding to correlated fluorescent signal would allow for a larger sampling pool. To reliably decide whether the obtained density corresponds to Ura7, an average resolution ranging from 5-10 Å would be needed to distinguish the alpha helixes

and beta sheets present in the structure **[Baker et al., 2007]**. However, because the location of the filament bundles corresponds to Ura7-GFP signal, a lower resolution that allows for reliable comparison of the average to the *in vitro* data reported by Hansen et al. would suffice **[Hansen et al., 2021]**.

Performance of subvolume-based template matching remains to be tested

Finally, a method was developed to enable STA of Ura2 and non-assembled Ura7. The template matching approach and associated coordinate transformations seemed theoretically successful, but subtomogram averages need to be obtained before one can gauge the reliability of the method. While the particle picking size limit for SPA generally fluctuates around 200 kDa, particle picking in tomographic data is much more prone to false positives due to the variety of potential candidates present in the biological material [**Rickgauer et al., 2017; Lucas et al., 2021**]. It remains an open-ended question whether PyTom-based template matching is even possible with particles of this size. Even so, the particles extracted do seem to resemble each other to some degree, indicating that the algorithm is picking up some repeating structure. Of course, this could merely reflect an unfortunate arrangement of noise or overall electron-dense areas. Metabolic enzymes are generally of a similar size to Ura2 and tetrameric Ura7, if not much smaller. Recent studies report pushing the size limit for template matching and could pose as suitable alternatives to the subvolume-based method in PyTom **[Rickgauer et al., 2017; Lucas et al., 2021]**. Equally, deep learning networks such as TomoTwin could prove useful once reliable functioning in experimental data is achieved (https://github.com/aniketkt/TomoTwin). In short, any robust method for picking metabolic enzymes would be a fruitful addition to the cryo-CLEM methodology developed in this study.

To conclude, Ura7 accumulates in *Saccharomyces cerevisiae* during starvation, most likely forming filaments to reduce enzymatic activity and slow metabolic growth. We speculate that the regulation of the CTP synthesis pathway is entirely controlled by Ura7, which carries out the rate-limiting step. Developing a cryo-CLEM methodology allowed for the identification and characterization of potential CTP synthase filaments *in situ*. While this method requires improvement, it lays the groundwork for enabling future investigation into the spatial organization of metabolic pathways.

Methods

Yeast cultivation

GFP-tagged yeast clones for genes YJL130C (Ura2) and YBL039C (Ura7) were obtained from the Yeast GFP Clone Collection (ThermoFisher Scientific). The clones were cultured on YPD 2% agar plates at RT for 2-3 days before storing at 4°C. Yeast liquid cultures were maintained in YPD medium. For inoculation, overnight cultures of yeast were diluted to an OD600 of 0.2 in YPD and grown shaking at 30°C for approximately 2 hours until early-mid log phase growth was reached.

Inducing filament formation

Overnight cultures of yeast were inoculated in YPD until early-mid log phase. Cells were harvested and washed in 1X PBA to remove any remaining nutrients. Starvation conditions were established by resuspending yeast cells in starvation buffer: 0.15 M phosphate-citrate buffer (pH 7). Subsequently, cultures were incubated for 30 minutes to 4 hours at 30°C while shaking.

Fluorescence microscopy

For obtaining initial FLM data of Ura7 accumulation in yeast, spinning disk confocal microscopy was performed using a FEI CorrSight microscope equipped with an Andromeda module. Z-stacks were collected using either a 40x 0.9 NA (EC Plan-Neofluar 40x/0.9 Pol M27, Zeiss) or a 20x 0.8 NA (EC Plan-Neofluar 20x/0.5 M27) dry objective. With a step size of 0.4 μm, 20 planes were acquired per site, resulting in a final stack thickness of 7.6 μm.

Quantitative analysis of fluorescence microscopy

A quantitative analysis of the Z-stacks obtained at different starvation timepoints was performed using Fiji, ImageJ **[Schindelin et al., 2012]**. A maximum intensity projection (MIP) of each Z-stack was smoothened (Process/Smooth, 3x3 neighborhood) and thresholded at a cutoff of 6323 or 0.36 % of the signal to create a binary image representing cell profiles (Image/Adjust/Threshold). After watershedding (Process/Binary/Watershed), particles were analyzed to determine the number of cells (Analyze/Analyze Particles). The roundness and size parameters used to exclude unwanted particles were not defined, as all particles corresponded to cells. To acquire the number of total GFP-foci, maxima were found in the original MIP of the Z-stack (Process/Find Maxima). Each image stack was processed using the same parameters. The total percentage of foci per total number of cells was calculated per condition, in addition to the lower and upper bounds of a binomial 95% confidence interval.

Western blot analysis

For Western blot analysis of the protein landscape of the yeast cultures, proteins were extracted through NaOH-aided lysis **[Kushnirov, 2000]**. Per 5.5 mL of 0.6 OD600 yeast culture, 200 μL 0.1 mM NaOH was added and incubated for 10 minutes at RT. Samples were spun down at 14,500x g for 1 minute, after which the NaOH supernatant was discarded. Lysates were flash frozen in liquid nitrogen and stored at -80°C until further use.

To determine the total protein concentration of the lysates prior to western blotting, a bicinchoninic acid assay (BCA) was performed using the BCA™ Protein Assay Kit (Pierce/ThermoFisher Scientific). Half of each sample lysate was thawed and resuspended in 100 μL 1X PBS. A custom python script was used to deduce the total protein concentration of each sample (Text S1).

20-25 μg of protein was loaded per lane on a 12% mini-PROTEAM TGX Precasted Gel (BioRad). Gels were run at 150 V (constant) and 50 mA for 50 minutes. Using the Trans-Blot Turbo System (BioRad), proteins were transferred from the gel to a TransBlot Turbo Transfer PVDF Membrane (BioRad) on a mixed molecular weight setting. After transfer, the membrane was cut to separate the target proteins from each other. The membrane segments were blocked in 0.05% milk in PBST (1X PBS with 0.005% Tween-20) for 30 minutes at RT. The blocking buffer was discarded, and the membranes were incubated with primary antibodies diluted in 0.05% milk PBST for 2 hours at RT. The following antibodies were used: anti-GFP rabbit IgG polyclonal antibody (Invitrogen: #A11122) at 1:2000 dilution; anti-beta actin rabbit polyclonal antibody (Life Technologies: #PA5-85271) at 1:2000 dilution; anti-Atg8 rabbit polyclonal antibody (Life Technologies: #PA1-26648) at 1:7000 dilution.

The membranes were washed by a quick rinse, then 5, 10, and finally 15 minutes of shaking in PBST. Next, the secondary antibody in 0.05% milk PBST was added. The membranes were incubated for 1 hour at RT and washed again according to the previously mentioned procedure. Anti-rabbit IgG HRP goat polyclonal antibody (Boster: BA1054-0,5) was used as the secondary antibody. To develop the blot, the ECL™ Prime Western Blotting Detection Reagents kit (Amersham) was used. Using the ChemiDoc XRS+ (BioRad), membranes were imaged through chemiluminescence at different exposure times (Supplementary).

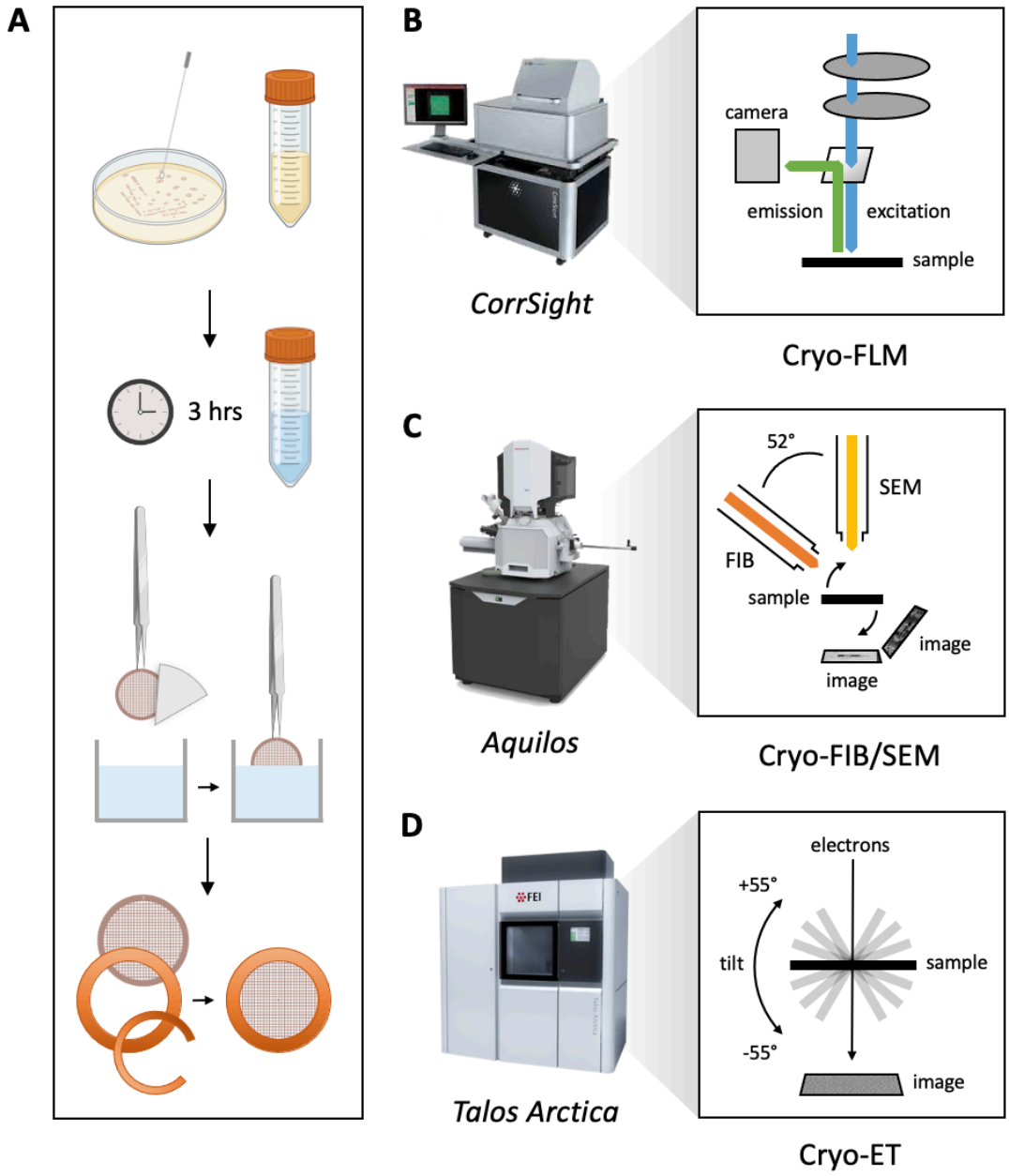

Figure 7: The cryo-CLEM sample preparation and data collection workflow.

(A) Yeast clones are cultivated on YPD agar plates or kept in liquid culture. Overnight liquid cultures are inoculated and incubated in starvation buffer for 3 hours. Grids with yeast sample are blotted and plunged into liquid ethane. Finally, vitrified grids are clipped into Autogrids. (B) Cryo-fluorescence light microscopy is performed on the samples using the FEI CorrSight microscope. (C) Samples are thinned to lamellae suitable for cryo-ET imaging using the Aquilos Cryo-FIB instrument. (D) Cryo-ET data is collected with the Talos Arctica electron microscope.

Vitrification

Samples for cryo-EM analysis were prepared by mixing green fluorescent Dynabeads (Invitrogen/ThermoFisher Scientific) into an aliquot of starved yeast culture with a ratio of 1:10. Using the PELCO easiGLOW (Ted Pella), 200 mesh copper R1/2 holey carbon grids (Quantifoil Micro

Tools) were glow discharged with a current of 45 mA for 45 seconds at 0.39 mBar. 3.25 µL of yeast sample was pipetted onto the charged grids and left to settle for 30 seconds. The grids were blotted from the back for 2 second after the initial moisture catch with Whatman 0.95 filter paper (Figure 7A). Immediately after, samples were vitrified in liquid ethane through manual plunging. The plunge frozen grids were clipped into AutoGrids (ThermoFisher Scientific) before proceeding with the cryo-CLEM workflow.

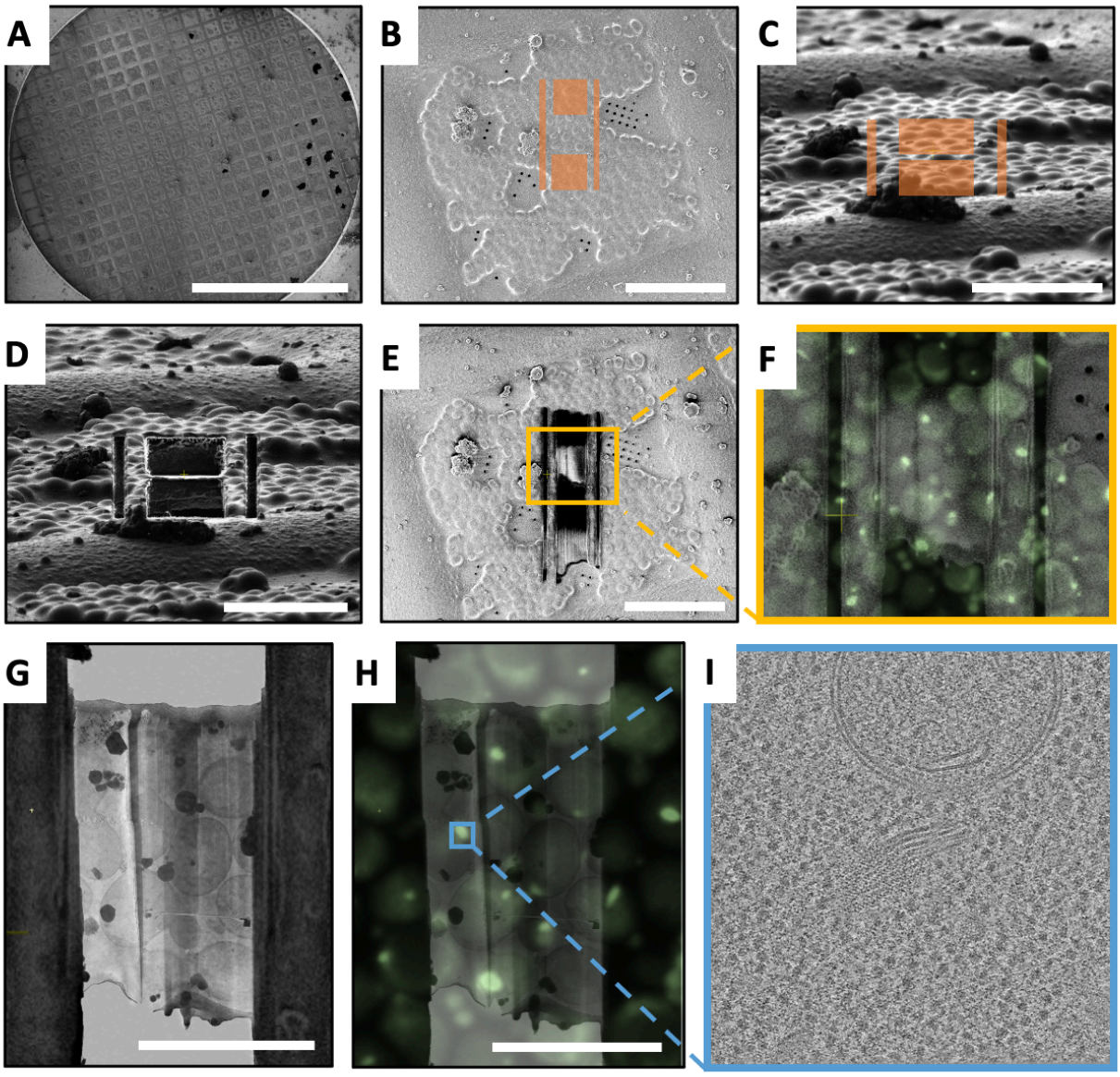

Figure 8: The cryo-FLM correlative method for sample preparation and tilt series recording.

(A) A SEM grid overview. Scale bar: 1 mm. (B & C) A SEM and FIB image of a grid square covered with vitrified yeast cells. The orange sections indicate the rough milling pattern position. Scale bar: 30 µm, 20 µm respectively. (D) A FIB image of the grid square after rough milling. (E) A SEM image of the final lamella after polishing. (F) The result of correlating the FLM data with the SEM image, based on the Dynabeads. (G) The SEM image of the lamella correlated with a stitched TEM overview. Scale bar: 10 µm. (H) Correlation of the FLM MIP with the TEM lamella overview. (I) A slice of the tilt series recorded at the site of the fluorescent signal indicated in H.

Cryo-fluorescence microscopy

For targeting both the thinning of the vitrified samples as well as the cryo-ET data collection, cryo-FLM data was acquired to identify the regions of interest by performing spinning disk confocal microscopy (Figure 7B). Grids were imaged using the FEI CorrSight microscope equipped with a cryo-stage cooled to liquid nitrogen temperature **[Arnold et al., 2016]**. Potential sites were selected in the FEI MAPS v3.8 software (ThermoFisher Scientific) and 30-plane thick Z-stacks with a 300 nm spacing were collected with a 40x 0.9 NA dry objective (EC Plan-Neofluar 40x/0.9 Pol M27, Zeiss). Collection was performed with an exposure time of 2000 ms per plane at 100% laser power. The excitation filter EX 488 nm was applied to excite both the GFP-tag and the Dynabeads in the target grid squares.

Cryo-FIB-milling

After collection of cryo-fluorescence data, samples were thinned to a suitable thickness for cryo-ET data collection using the FEI Aquilos Cryo-FIB dual-beam microscope (ThermoFisher Scientific) (Figure 7C). From the potential targets selected during cryo-FLM, grid squares were selected based on the integrity of the carbon film and the degree to which the buffer was blotted away. The grids were coated with a layer of platinum to reduce charging effects (10 sec, 10 Pa, 30 mA, 1 kV). The deposition of a second layer of organometallic platinum via a gas injection system (GIS) served to protect the surface of the sample from damage and limit curtaining artefacts. The imaging process was guided by FEI MAPS v3.8 software. Grid overviews were acquired at mapping position both pre-coating and post-coating with scanning electron microscopy (SEM) (Figure 8A). Eucentric height was determined per target grid square, as well as the optimal milling angle, ranging from 16 to 20° stage tilt. The sites were milled in a stepwise fashion, with each consecutive step employing a lower Ga^+ beam current (1 nA, 0.3 nA, 0.1 nA, 30 pA). The exact placement of the rough milling pattern was dictated by both the number of GFP foci observed in the corresponding Z-stacks as well as the estimated stability and size of the lamellae (Figure 8B/C). In between the fine milling and polishing steps, a high-resolution SEM image (1536 x 1024, 1 us, 1000x magnification) was acquired at mapping position (sample perpendicular to the electron column) for CLEM-correlation purposes prior to cryo-ET (Figure 8E).

Correlation of FLM and SEM data

Before FLM-guided tilt series collection, acquired FLM and SEM images of the lamellae were correlated. Using the 3D Correlation Toolbox, Z-stack were resliced and Dynabeads were manually selected in both FLM and SEM images **[Arnold et al., 2016]**. Scaling, translation, and rotation factors were calculated with the toolbox. Using a python script, the FLM images were scaled, translated, and rotated to match the SEM views (Text S2, Figure 8F). Actual overlay of the images was performed in ImageJ.

FLM-guided tilt series collection

Following sample preparation, lamellae were transferred to a FEI Talos Arctica transmission electron microscope (200 kV, ThermoFisher), fitted with a K2 direct camera and a Gatan filter for cryo-ET data collection (Figure 6D). In SerialEM, low-magnification maps were collected of the lamellae at 4,800x

magnification resulting in a pixel size of 38.6 Å/px. The maps were exported, and stitching was improved in IMOD's Etomo module if necessary **[Mastronarde & Held et al., 2017]**. Through manual scaling and alignment based on shape outline and distinctive landmarks, a correlation of the SEM lamellae overview with the TEM map was constructed (Figure 8G). Consequently, the FLM-data could be overlayed with the TEM view, as per the previously determined SEM-FLM correlation (Figure 8H). Dose-symmetric tilt series were recorded at the sites of fluorescent signal, at 42000x magnification with a pixel size of 2.17 Å/px, defocus of 3 μm, and a 2° increment. A total dose of approximately 100 $e^-/Å^2$ was reached over the total tilt range of -55 to 55° (non-relative to the FIB-SEM stage tilt).

Tomogram reconstruction

The collected tilt series were first aligned using alignframes (IMOD) and then reconstructed in IMOD/4.10.44a's Etomo module **[Mastronarde & Held et al., 2017]**. After coarse alignment, fine alignment of the tilts was performed via patch tracking. CTF estimation of the tilts was performed using the IMOD CTF plotter, fitting up to 5 zeros at a defocus of approximately 3 μm. Subsequently, CTF correction by phase-flipping was performed using ctfphaseflip. The final aligned images were binned by a factor of 2. Finally, the tomograms were reconstructed using weighted back-projection with a SIRT-like filter representing 5 iterations. The resulting tomograms had a pixel size of 4.34 Å/px.

Filament averaging

To elucidate the structure of the filaments observed, filament averaging was performed. The filaments were manually picked in 3dmod (IMOD), with contours tracking the curvature and progression of the filaments in all dimensions. After selection of the filaments, the model was processed using addModPts (PEET/1.13.0) **[Heumann et al., 2011]**. With a constant size interval of 4 nm, points were added along the contours (Figure 9A). Each point in this model represented the center of a particle. Using IMOD/PEET's Subvolume Averaging package for averaging particles, the newly created model was processed. Boxes with a size of 36:36:36 were centered around each point, essentially extracting the particles. Initial determination of the structure was performed without a reference, to avoid bias. After it was confirmed that the raw average resembled Ura7, the particles were averaged with both a reference and/or a mask. The reference was obtained from the Ura7 filament structure determined by Hansen et al. and inverted, scaled, and clipped to a boxsize of 36:36:36 pixels with a pixel size of 4.34 Å/px using EMAN2/2.91 (Figure S4) **[Hansen et al., 2021]**. The cylindrical mask was created in EMAN2 as well and then softened in RELION/3.1.2.

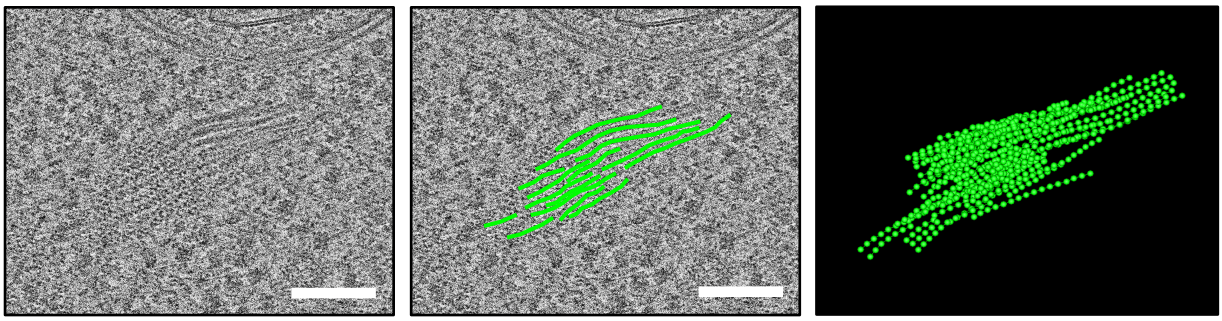

Figure 9: Picking and averaging the repeating unit of the filament bundles.

The model picking strategy is visualized in green. Contours were placed to trace the general shape of the filaments. Points were added to essentially pick the particles from the model. Scale bar: 200 nm.

Subvolume-based template matching

Subtomogram averaging (STA) of Ura2 and Ura7 was performed in PyTom (development version, https://github.com/FridoF/PyTom). Before STA of the proteins of interest could be executed, customization of the standard PyTom STA workflow was necessary. Firstly, the IMOD-reconstructed volumes had to be imported into PyTom by use of the SerialEM mdoc-file generated per tilt series. The patch tracking model generated in IMOD was transformed into a PyTom-style markerfile, with the marker coordinates corresponding to the positions of the patches. Using weighted back projection, reconstruction of non-CTF corrected projections was performed, with a binning factor of 4 (8.68 Å/px). Consequently, particles were picked via template matching in the PyTom-generated volumes. Considering the limited molecular mass of both Ura2 and Ura7, template match had to be run with high magnification tomograms not optimally binned. To account for the increase in memory utilized by the larger volume and to maximize processing efficiency, the tomogram was split up into subvolumes (Figure 10A). The splitVolumes function in PyTom (pytom/localization/parallel_extract_peaks/PeakLeader/splitVolumes) was customized, rewriting the parallel_extract_peaks.py PyTom script (Text S3), with the purpose of writing the subvolumes as well as corresponding job and bash execution files to disk. A custom python script was written to access and run the adjusted splitVolumes function (runSplitVolumes2.py, Text S4). Use of GNU parallel commands enabled consecutive execution of the numerous subvolume template matching bash files. By virtue of the parallel command, the template matching runs were submitted to the GPU for optimal processing efficiency without requiring manual supervision or intervention.

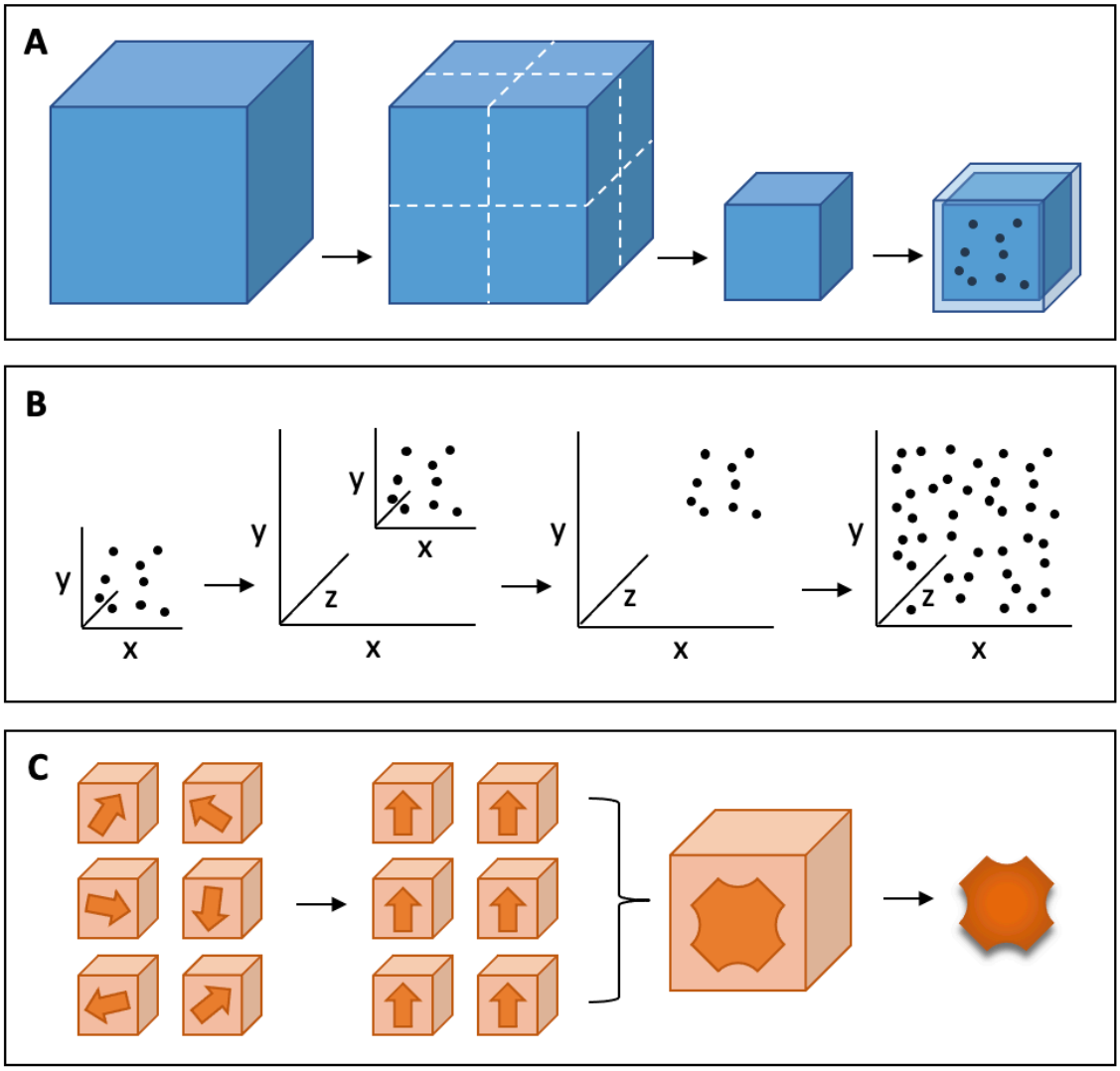

Figure 10: The subvolume-based approach to template matching.

(A) The dividing of the full tomogram volume up into subvolumes. For template matching, the particle picking space of the subvolume is expanded by half the size of the reference. (B) The picked particles have to be plotted back into the coordinate system of the original volume. Using a translation, particle coordinates can be accurately retrieved and the picks of the different subvolume can be combined in one particle list. (C) The proposed STA approach after extraction and transformation of the particles. First, subtomograms are reconstructed from the original projections. Subtomograms are aligned and classified to finally obtain an average.

The Ura2 structure used for template matching was generated from its AlphaFold structure (https://alphafold.ebi.ac.uk/entry/P28274). In Chimera/1.12, a density map was generated from the molecular structure using the "molmap" command, mimicking a resolution of 3 Å. Using EMAN2/2.91, the resulting density was inverted, clipped, and scaled to match the pixel spacing of the subvolumes (8.68 Å/px). The mask was also produced in EMAN2, with a soft edge.

After the scores and angles files were generated, particles were extracted using a bash loop. However, since the subvolume were treated like separate tomograms, the coordinates of the particles found were relative to the coordinate system of the subvolume. Through a python script (rewriteParticles.py, Text S5) executed by a shell script, the particles were therefore plotted back into the coordinate system of the original volumes (Figure 10B). Concurrently, particle filenames were rewritten, as reconstructed subtomograms would otherwise overwrite each other. The number of candidate particles extracted was estimated at the hand of the total number of molecules present in the volume of the cell. For Ura2, this amounted to extraction of 200 particles per subtomogram (https://www.yeastgenome.org/locus/S000003666/protein). The new particle lists were combined in the PyTom GUI.

Supplementary Materials

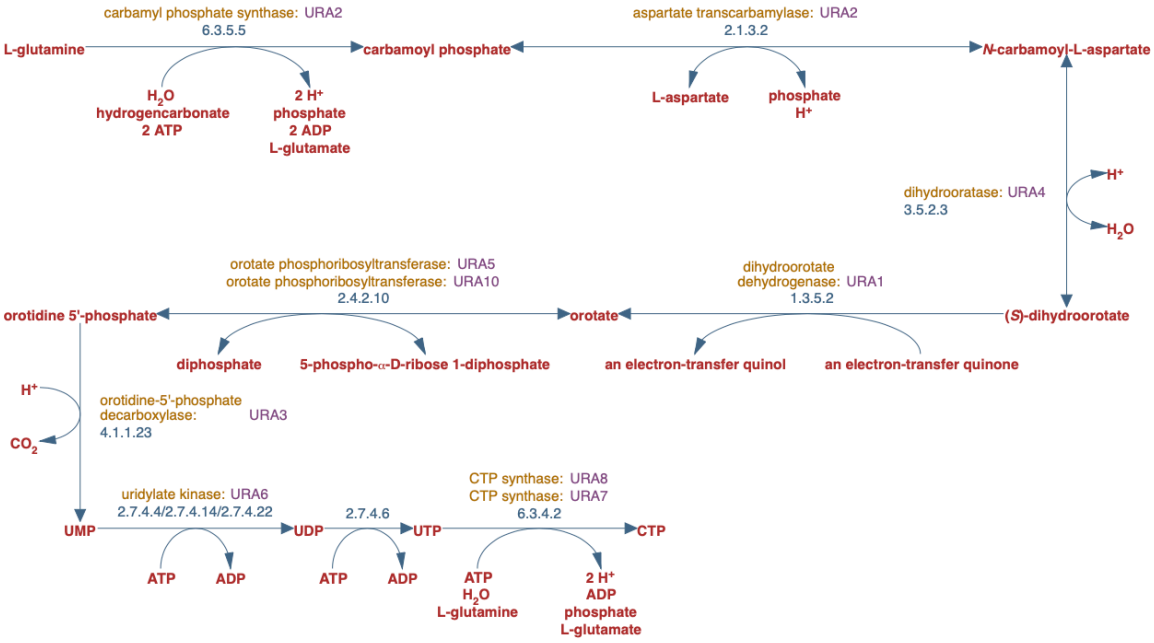

***Figure S1: The CTP synthesis pathway in* S. cerevisiae.**

Enzymes are given in yellow; metabolic substrates, products, and cofactors in red; names of the enzymes in S. cerevisiae *in purple.*

Saccharomyces cerevisiae UTP and CTP de novo biosynthesis. Retrieved September 16, 2022, from https://pathway.yeastgenome.org/YEAST/NEW-IMAGE?type=PATHWAY&object=PWY-7176

A

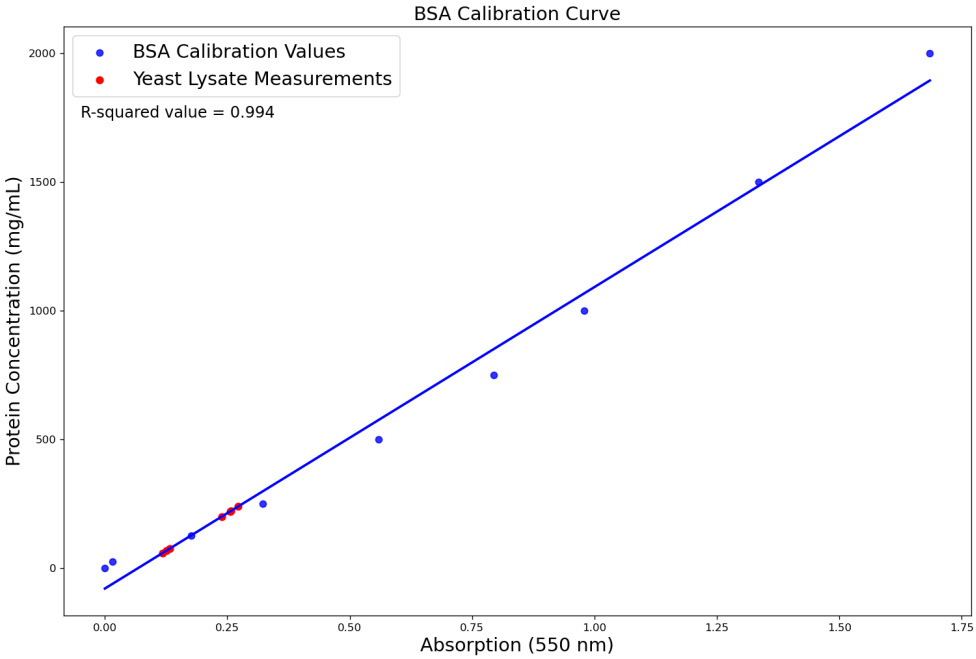

B

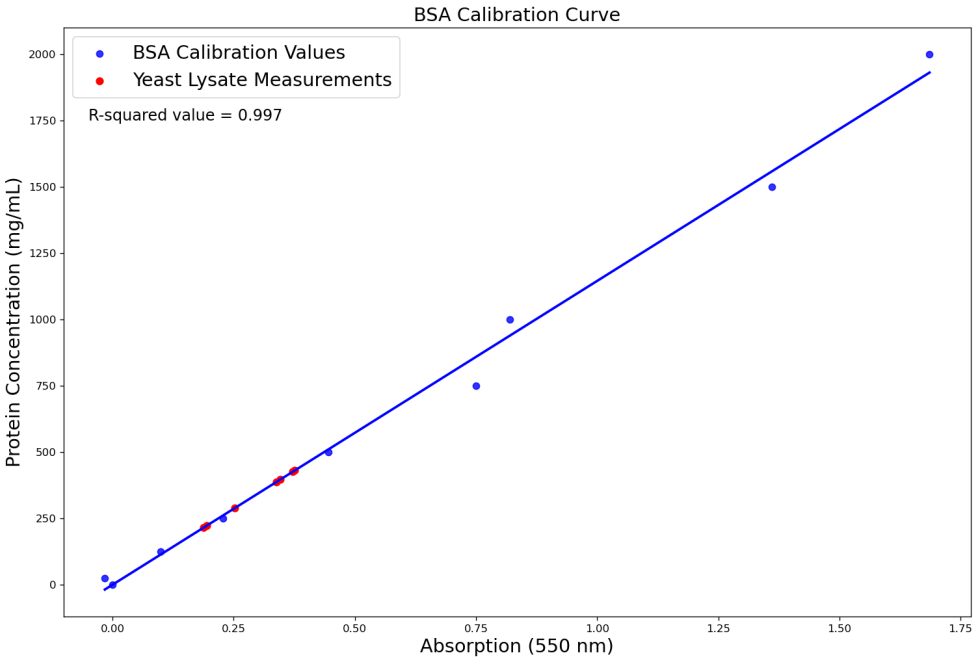

Figure S2: BSA analysis shows that overall protein concentrations are similar in both log phase growth and starvation states of the cells.

(A & B) The left cluster of red points represents an 8 times dilution of the lysates. The right cluster corresponds to a 4 times dilution of the samples.

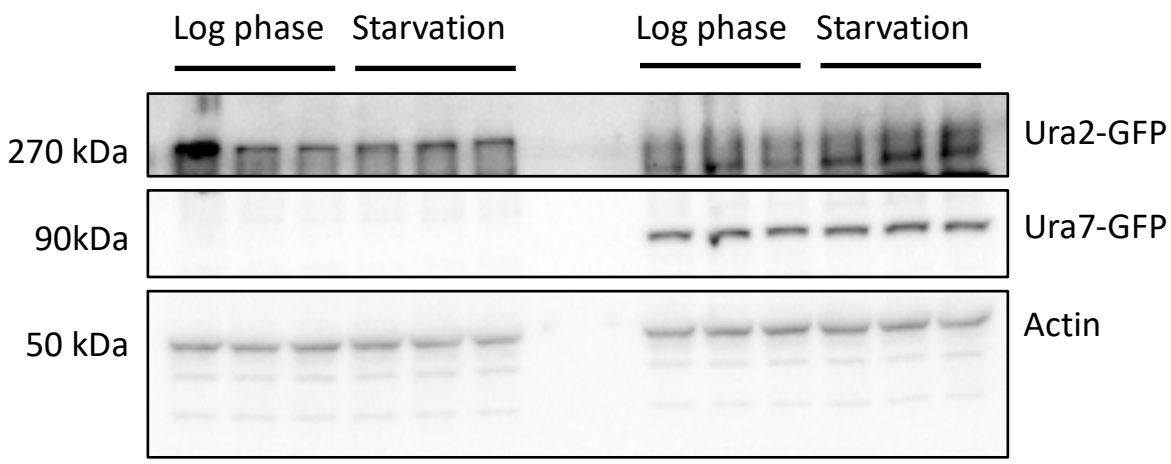

Figure S3: The repeat of the western blot analysis displays similar results.

Western blot analysis of the protein lysates shows that Ura2 and Ura7 expression levels are relatively unchanged by starvation stress.

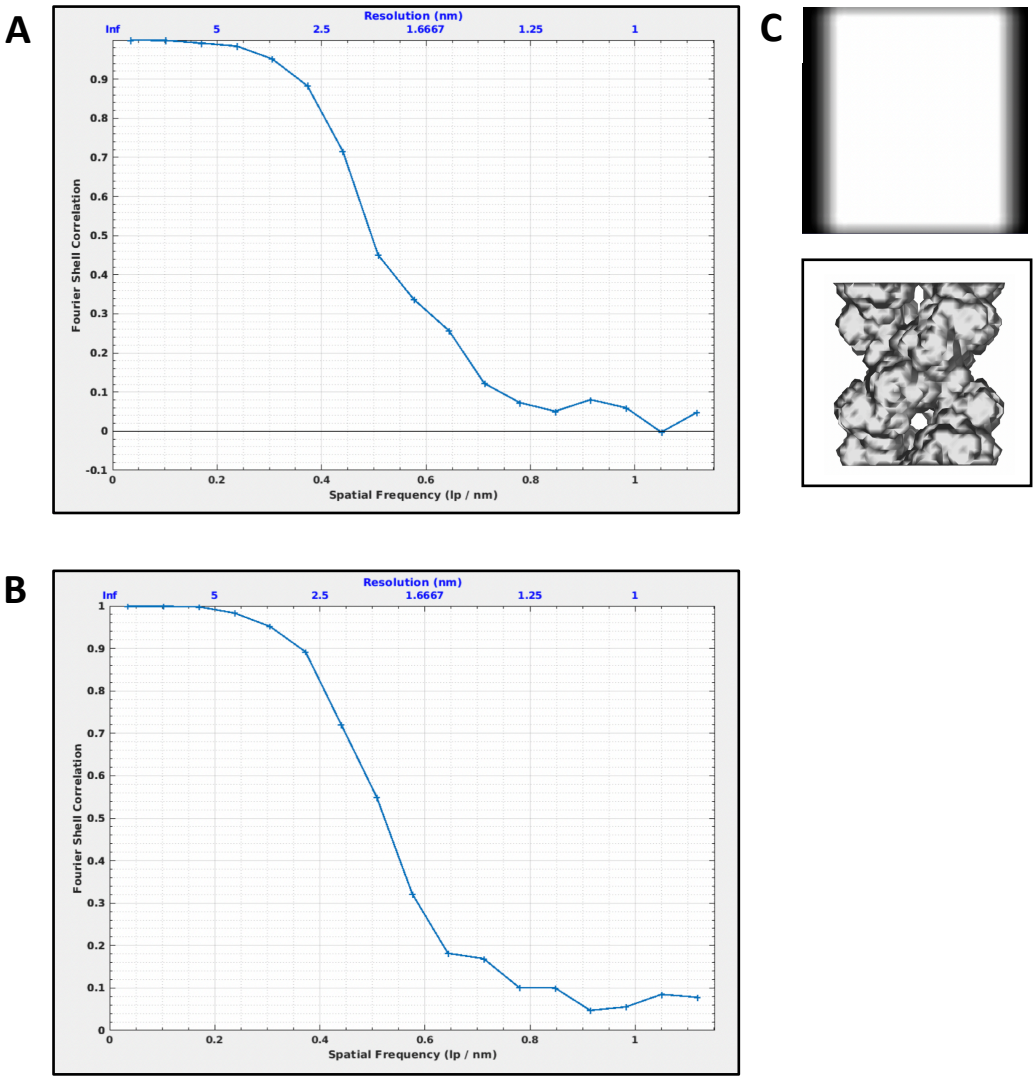

Figure S4: Filament averaging was performed and the resulting averages were low pass filtered according to their resolution.

(A) The Fourier shell correlation curve of the average obtained from run039. (B) The Fourier shell correlation curve of the average obtained from run041. (C) The mask used for both run039 and run041, in addition to the reference generated from the in vitro structure of Ura7.

Table S1: Quantification of the fluorescence microscopy experiment.

Lower and upper bound 95% confidence intervals were calculated for a binomial distribution.

Timepoint (min)	Fluorescent Protein	Cells	Maxima	Percentage	Lower Bound 95% CI	Upper Bound 95% CI
30	Ura2	1,463	10	0.68	0.00	0.01
60	Ura2	1,069	15	1.40	0.01	0.02
120	Ura2	1,697	11	0.65	0.00	0.01
180	Ura2	1,653	7	0.42	0.00	0.01
240	Ura2	1,321	6	0.45	0.00	0.01
30	Ura7	1,766	421	23.84	1.94	2.06
60	Ura7	1,160	459	39.57	2.87	2.93
120	Ura7	1,912	1205	63.02	2.22	2.18
180	Ura7	2,370	1658	69.96	1.86	1.84
240	Ura7	3,297	2321	70.40	1.60	1.60

Table S2: The total protein concentrations determined for each lysate of Figure ?1.

Lysate	Growth Phase	Concentration (μg/μL)
Ura2	Log phase	1.384
Ura2	Starvation	1.352
Ura7	Log phase	1.488
Ura7	Starvation	1.504

Table S3: The total protein concentrations determined for each lysate of Figure S1.

Lysate	Growth Phase	Concentration (μg/μL)
Ura2	Log phase	1.018
Ura2	Starvation	0.950
Ura7	Log phase	1.076
Ura7	Starvation	1.044

Table S4: The exposure times used to visualize the protein bands during western blot analysis.

Target protein	Antibody	Exposure time (s) Figure 3	Exposure time (s) Figure S1
Ura2	Anti-GFP	10	4
Ura7	Anti-GFP	60	20
Actin	Anti-actin	40	20
Atg8	Anti-Atg8	180	50

Table S5: The different parameters of the filament averaging jobs run.

Run	Reference	Mask	Search Distance	Phi	Theta	Psi
036	Particle 2184	-	5	180	30	20
039	Ura7 filament	Cylindrical	4	180	30	20
040	Particle 2184	Cylindrical	5	180	30	20
041	Particle 777	Cylindrical	5	180	30	20
043	Average run 041	Cylindrical	3	180	30	20
044	Average run 043	Cylindrical	5	180	30	20

Text S1: Custom python script for analyzing BCA measurements.

```
#!/usr/bin/env python

# open text file with BCA values
BCA = open("BCA_0606.txt", "r")

bca = {}

# read lines in file into dictionary
for line in BCA:
   line = line.rstrip()
   term = line.split("|")
   bca[term[0]] = float(term[1])

BCA.close()

# account for the blank
blank = bca["I"]

for key in bca:
   bca[key] = bca[key] - blank

# separate values based on experiment
calibration = {}
measurement = {}

for key in bca:
   if key[0] == "U":
      measurement[key] = bca[key]
   else:
      calibration[key] = bca[key]

# print(measurement, "\n", calibration)

# change calibration keys to concentration BSA
concentration = [2000, 1500, 1000, 750, 500, 250, 125, 25, 0]
index = -1
cal = {}

for key in calibration:
   index += 1
   cal[concentration[index]] = calibration[key]
# print(cal)

# separate calibration values and keys for seaborn plot
calval = []
calkey = []
for key in cal:
   calval.append(cal[key])
   calkey.append(key)
```

```
# plot and fit calibration curve
import matplotlib.pyplot as plt
import seaborn as sns

plt.figure(figsize = (15, 10), dpi = 120, facecolor = "w", edgecolor = "k")
sns.regplot(x = calval, y = calkey, data = cal, ci = None, label = "BSA Calibration Values", color = "b",
marker = "o")
plt.title("BSA Calibration Curve", fontsize = "xx-large")
plt.ylabel("Protein Concentration (mg/mL)", fontsize = "xx-large")
plt.xlabel("Absorption (550 nm)", fontsize = "xx-large")

# get the equation
from scipy.stats import linregress

slope, intercept, r_value, p_value, std_err = linregress(calval, calkey)

def fitline(b):
   return intercept + slope * b

# calculate the measurement concentrations
measured = {}
for key in measurement:
   measured[measurement[key]] = fitline(measurement[key])
print(measurement)
print(measured)

# plot the measurement points
plt.scatter(measured.keys(), measured.values(), label = "Yeast Lysate Measurements", color = "r",
marker = "o")
plt.annotate("R-squared value = {:.3f}".format(r_value), (-0.05, 1750), fontsize = "x-large")

index = -1
for key in measured:
   index += 1
   plt.annotate(list(measurement.keys())[index], (key, measured[key]))
plt.legend(fontsize = "xx-large")
```

Text S2: Python script for applying the coordinate transformations calculated by the 3D correlation toolbox.

```
#! /cm/shared/apps/miniconda2/envs/pyto/bin/python3

module load miniconda/pyto/1.6.0
condaactivate
ipython

'''
   "This example shows how to apply a coordinate transformation previously obtained by correlating
   "a 3D (such as confocal) and a 2D (such as ion beam) image to transform the correlated
   "images. In this way, the confocal image is transformed to the ion beam coordinate
   "system, so that the transformed confocal image "looks like" the ion beam image, or
   "the ion beam image is transformed to the confocal system.

   "The transformation is read from the output files previously generated by running 3DCT.
   "To make it easier to visualize the transformation, the images used to establish the
   "correlation were artificially generated.
   "
   "The image transformations shown here are performed using Pyto package."
'''
import pyto
import sys
import pickle
from copy import copy, deepcopy
import numpy as np
import tifffile as tf
import pyto
from pyto.geometry.rigid_3d import Rigid3D
import matplotlib as mpl
import matplotlib.pyplot as plt

confocal_file_name = 'S3L12FLM_resliced.tif'
ion_beam_file_name = 'S3L12SEM.tif'
#ion_beam_size = [1024,941] #x,y Should add programatic extraction
results_file_name = 'S3L12XYZ_full.txt'
results_file_name_min = 'S3L12XYZ.txt'

# Read images and adjust axes
cf_data = tf.imread(confocal_file_name).transpose()
confocal_size=cf_data.shape
ib_data = tf.imread(ion_beam_file_name)
if len(ib_data.shape) == 3:
   ib_data = ib_data[:,:,0]
ib_data = ib_data.transpose()

# read marker positions
results = np.loadtxt(results_file_name_min)
#print(results)
cf_markers = results[:,0:3]
cf_markers_transformed = results[:,3:6]
```

```
ib_markers = results[:,6:8]
transform_error = results[:,8:10]

# Read parameters from 3DCT results
with open(results_file_name, 'r') as results_fd:
   for line in results_fd:
      if line.startswith('#   - rotation'):
         phi, psi, theta = np.fromstring(line.split(': [')[1].split(']')[0], sep=',')
         continue
      if line.startswith('#   - scale'):
         scale = float(line.split('= ')[1])
         continue
      if line.startswith('#   - translation for rotation around [0,0,0]'):
         trans = np.fromstring(line.split('= [')[1].split(']')[0], sep=',')
         continue
      if line.startswith('#   - translation for rotation around'):
         origin = np.fromstring(line.split('[')[1].split(']')[0], sep=',')
         trans_or = np.fromstring(line.split('= [')[1].split(']')[0], sep=',')
         break

print("Please check that the following parameters are the same as those in the 3DCT results file:")
print("phi, theta, psi = {}".format((phi, theta, psi)))
print("scale = {}".format(scale))
print("translation around [0, 0, 0] = {}".format(trans))
print("translation around {} = {}".format(origin, trans_or))


# Make transformation from confocal to ion beam (based on 3DCT correlation results)
euler_rad = np.array([phi, theta, psi]) * np.pi / 180
#q = pt.Rigid3D.make_r_euler(angles=euler_rad)
q = Rigid3D.make_r_euler(angles=euler_rad) #Original line
tdct = Rigid3D(q=q, scale=scale, d=trans) #Original line
#tdct = Rigid3D()
#tdct.gl=q
#tdct.s=scale
#tdct.d=trans #, d=trans)

# reposition so that transformed markers z > 0
cf_markers_tf = tdct.transform(x=cf_markers, xy_axes='point_dim') #Original line
#cf_markers_tf = af.Affine.transform(tdct,x=cf_markers, xy_axes='point_dim')
tdct_z = deepcopy(tdct)
tdct_z.d[2] += -np.floor(cf_markers_tf[:,2]).min()
tdct_z.transform(x=cf_markers, xy_axes='point_dim')

# Transform confocal image
# Pad the confocal image to prevent chopping
padded=(1600,1200,1000)
cf_data_tf = tdct_z.transformArray(array=cf_data,shape=padded)
#cf_data_tf should also be saved as 3d file

#save as maxproj.tiff
```

```
cf_tf_file_name = 'S3L12Z_max.tif'
data = cf_data_tf.max(axis=2).transpose()
#sum instead of max sometimes is better
# data = cf_data_tf.sum(axis=2).transpose()
pixel_um = 0.164
cf_meta = {"PixelSize": str(pixel_um), "FocusStepSize": str(pixel_um)}
cf_res = (10000/pixel_um, 10000/pixel_um, 'CENTIMETER')
tf.imsave(cf_tf_file_name, data, metadata=cf_meta, resolution=cf_res)
```

Text S3: Rewritten version of the splitVolumes function for writing subvolumes and corresponding job files to disk.

```
def splitVolumes2(self, job, splitX, splitY, splitZ, filename, gpuID, verbose=True):
    """
    splitVolumes: Split the target volume in job into smaller ones and write subjobs and volumes to disk.
    """
    # check if the split is feasible
    v = job.volume.getVolume()
    r = job.reference.getVolume()

    print(r.sizeX(), r.sizeY())

    vsizeX = v.sizeX(); vsizeY = v.sizeY(); vsizeZ = v.sizeZ()
    sizeX = vsizeX//splitX; sizeY = vsizeY//splitY; sizeZ = vsizeZ//splitZ
    rsizeX = r.sizeX(); rsizeY = r.sizeY(); rsizeZ = r.sizeZ()
    if rsizeX>sizeX or rsizeY>sizeY or rsizeZ>sizeZ:
       raise RuntimeError("Not big enough volume to split!")

    self.jobInfo["originalSize"] = [vsizeX, vsizeY, vsizeZ]
    self.jobInfo["splitSize"] = [sizeX, sizeY, sizeZ]

    # read the target volume, calculate the respective subregion
    from pytom.localization.peak_job import PeakJob
    from pytom.localization.structures import Volume
    _start = [-rsizeX//2,-rsizeY//2,-rsizeZ//2]
    _size = [sizeX+rsizeX, sizeY+rsizeY, sizeZ+rsizeZ]

    # obtain original reference name (not path)
    orig_ref_name = job.reference.getFilename()

    # write a textfile for storing the subvolume coordinates
    textfile = "subRegions" + "_" + filename[:-4] + ".txt"
    txt = open(textfile, "w")

    for i in range(splitX*splitY*splitZ):
       strideZ = splitX*splitY; strideY = splitX
       incZ = i//strideZ; incY = (i%strideZ)//strideY; incX = i%strideY
       _start = [-rsizeX//2+incX*sizeX,-rsizeY//2+incY*sizeY,-rsizeZ//2+incZ*sizeZ]

       start = _start[:]
       end = [start[j]+_size[j] for j in range(len(start))]

       if start[0] < 0:
          start[0]=0
       if start[1] < 0:
          start[1]=0
       if start[2] < 0:
          start[2]=0
       if end[0] > vsizeX:
```

```
    end[0] = vsizeX
if end[1] > vsizeY:
    end[1] = vsizeY
if end[2] > vsizeZ:
    end[2] = vsizeZ

size = [end[j]-start[j] for j in range(len(start))]

# for reassembling the result
whole_start = start[:]
sub_start = [0, 0, 0]
if start[0] != 0:
    whole_start[0] = start[0]+rsizeX//2
    sub_start[0] = rsizeX//2
if start[1] != 0:
    whole_start[1] = start[1]+rsizeY//2
    sub_start[1] = rsizeY//2
if start[2] != 0:
    whole_start[2] = start[2]+rsizeZ//2
    sub_start[2] = rsizeZ//2
self.jobInfo[i+1] = [sub_start, whole_start]

# writing the filenames for each subvolume
jobfilename = filename[:-4] + "_sub" + str(i) + ".xml"
volfilename = filename[:-4] + "_sub" + str(i) + ".mrc"
bashfilename = filename[:-4] + "_sub" + str(i) + ".sh"

subregion = [start[0], start[1], start[2], size[0], size[1], size[2]]

# create an actual volume
subVol = Volume.getVolume(job.volume, subregion = subregion)

print("This is the subregion of subvolume " + str(i) + ".")
print(subregion)
txt.write(str(subregion))
txt.write("\n")

# write volume to disk
from pytom.basic.files import write_em

mrc = write_em(volfilename, subVol)

# replace original tomogram with newly generated subvolume
path2mrc = job.dstDir + volfilename
subVol2 = Volume(path2mrc, [0,0,0,0,0,0])

import os

# write a reference link per subvolume
# to avoid overwriting
ref_link = orig_ref_name[:-4] + "_sub" + str(i) + ".mrc"
```

```
        os.symlink(orig_ref_name, ref_link)
        job.reference.setFilename(filename = ref_link)

        # write subjob file to disk
        subJob = PeakJob(subVol2, job.reference, job.mask, job.wedge, job.rotations, job.score, i+1,
dstDir = job.dstDir, bandpass = job.bandpass)
        xml = subJob.toXMLFile(jobfilename)

        # write shell script to disk
        path2xml = job.dstDir + jobfilename

        def subRunscript(filename, jobFile, gpuID):
            from pytom.tools.files import dump2TextFile

            text = "#!/bin/bash\n"
            text += "cd " + job.dstDir + "\n" + "\n"
            text += "mpiexec --tag-output -n 1 " + "/data/gijsvds/pytom-
develop/gui_devel/pytom/bin/pytom /data/gijsvds/pytom-
develop/gui_devel/pytom/bin/localization.py" + " -j " + jobFile + " --gpuID " + str(gpuID) + "\n"
            dump2TextFile(filename, text, append = False)

        subRunscript(bashfilename, path2xml, gpuID = gpuID)
```

Text S4: Custom python script for accessing the splitVolumes2 function (runSplitVolumes2.py)

```
#!/usr/bin/env pytom

# run like so:
# pytom runSplitVolumes2.py [job file] [splitX] [splitY] [splitZ] [gpuID]

verbose = True

import parallel_extract_peaks2 as pp2
from pytom.localization.peak_job import PeakJob
import os
import sys
import operator

filename = sys.argv[1]
job = PeakJob()
job.fromXMLFile(filename)
job.check()

X = int(sys.argv[2])
Y = int(sys.argv[3])
Z = int(sys.argv[4])

gpuID = sys.argv[5]

peak = pp2.PeakManager()

peak.splitVolumes2(job, splitX = X, splitY = Y, splitZ = Z, filename = filename, gpuID = gpuID)
```

Text S5: Custom python script for transforming extracted particles back into their original coordinate system.

```
#!/usr/bin/env pytom

# run using the rewriteParticles.sh bash script for multiple particle lists

verbose = True

import numpy as np
from pytom.basic.structures import ParticleList
import sys
import operator
import copy

# create particle list structures
pl = ParticleList()
new_pl = ParticleList()

# load sub particle list into variable
filename = sys.argv[1]
pl.fromXMLFile(filename)

from pytom.basic.structures import PickPosition
from pytom.basic.structures import Particle

# read in the subregion for the correct subvolume
with open(sys.argv[4]) as txt:
   subregions = txt.read().splitlines()

substarts = []

for line in subregions:
   listified = line.strip("][").split(",")

   startX = listified[0]
   startY = listified[1]
   startZ = listified[2]

   substart = [startX, startY, startZ]
   substarts.append(substart)

index = int(sys.argv[3])

regionX = int(substarts[index][0])
regionY = int(substarts[index][1])
regionZ = int(substarts[index][2])

print(regionX, regionY, regionZ)

for p in pl:
```

```
    subCoordinates = p.getPickPosition()
    # retrieve coordinates of the particle
    subX = subCoordinates.getX()
    subY = subCoordinates.getY()
    subZ = subCoordinates.getZ()
    #print(subCoordinates)

    # transform coordinates back into the whole tomogram
    newX = subX + regionX
    newY = subY + regionY
    newZ = subZ + regionZ

    # create new PickPosition variable with the new coordinates
    newCoordinates = copy.deepcopy(subCoordinates)
    newCoordinates.setX(newX)
    newCoordinates.setY(newY)
    newCoordinates.setZ(newZ)

    # rewrite particle name to avoid overriding during STA
    oldname = p.getFilename()
    newname = oldname[:-3] + "_sub" + sys.argv[3] +".em"

    # create a new particle from the old particle
    # but replace the PickPosition with the one containing the new coordinates
    new_p = copy.deepcopy(p)
    new_p.setPickPosition(newCoordinates)
    new_p.setFilename(newname)

    #add the new particle to the new particle list
    new_pl.append(new_p)

output = filename[:-4] + "_transformed.xml"
new_pl.toXMLFile(output)
```

```
#!/bin/bash
# run in TM directory
# run like so:
# bash rewriteParticles.sh reference subregions_textfile

for i in {0..15}
do
	pytom /data/stuart/Flory/CTPsynthase/pytom/subvolumes/method/rewriteParticles.py
particles_TM_job2_sub$i.xml $1 $i $2
done
```

References

Antonelli, R., Estevez, L., & Denis-Duphil, M. (1998). Carbamyl-phosphate synthetase domain of the yeast multifunctional protein Ura2 is necessary for aspartate transcarbamylase inhibition by UTP. *FEBS Letters*, *422*(2), 170–174. https://doi.org/10.1016/s0014-5793(98)00010-6

Arnold, J., Mahamid, J., Lucic, V., De Marco, A., Fernandez, J. J., Laugks, T., Mayer, T., Hyman, A., Baumeister, W., & Plitzko, J. (2016). Site-Specific Cryo-focused Ion Beam Sample Preparation Guided by 3D Correlative Microscopy. *Biophysical Journal*, *110*(4), 860–869. https://doi.org/10.1016/j.bpj.2015.10.053

Baker, M. L., Ju, T., Chiu, W. (2007). Identification of Secondary Structure Elements in Intermediate Resolution Density Maps. *Structure, 15*(1), 7–19. https://doi.org/10.1016/j.str.2006.11.008

Barros, L. F., & Martínez, C. (2007). An Enquiry into Metabolite Domains. *Biophysical Journal*, *92*(11), 3878–3884. https://doi.org/10.1529/biophysj.106.100925

Barry, R. M., Bitbol, A. F., Lorestani, A., Charles, E. J., Habrian, C. H., Hansen, J. M., Li, H. J., Baldwin, E. P., Wingreen, N. S., Kollman, J. M., & Gitai, Z. (2014). Large-scale filament formation inhibits the activity of CTP synthetase. *eLife*, *3*. https://doi.org/10.7554/elife.03638

Bauler, P., Huber, G., Leyh, T., & McCammon, J. A. (2010). Channeling by Proximity: The Catalytic Advantages of Active Site Colocalization Using Brownian Dynamics. *The Journal of Physical Chemistry Letters*, *1*(9), 1332–1335. https://doi.org/10.1021/jz1002007

Carcamo, W. C., Satoh, M., Kasahara, H., Terada, N., Hamazaki, T., Chan, J. Y. F., Yao, B., Tamayo, S., Covini, G., von Mühlen, C. A., & Chan, E. K. L. (2011). Induction of Cytoplasmic Rods and Rings Structures by Inhibition of the CTP and GTP Synthetic Pathway in Mammalian Cells. *PLoS ONE*, *6*(12), e29690. https://doi.org/10.1371/journal.pone.0029690

Castellana, M., Wilson, M. Z., Xu, Y., Joshi, P., Cristea, I. M., Rabinowitz, J. D., Gitai, Z., & Wingreen, N. S. (2014). Enzyme clustering accelerates processing of intermediates through metabolic channeling. *Nature Biotechnology*, *32*(10), 1011–1018. https://doi.org/10.1038/nbt.3018

Cohen, R. D., & Pielak, G. J. (2017). A cell is more than the sum of its (dilute) parts: A brief history of quinary structure. *Protein Science*, *26*(3), 403–413. https://doi.org/10.1002/pro.3092

French, J. B., Jones, S. A., Deng, H., Pedley, A. M., Kim, D., Chan, C. Y., Hu, H., Pugh, R. J., Zhao, H., Zhang, Y., Huang, T. J., Fang, Y., Zhuang, X., & Benkovic, S. J. (2016). Spatial colocalization and functional link of purinosomes with mitochondria. *Science*, *351*(6274), 733–737. https://doi.org/10.1126/science.aac6054

Gaertner, F. (1978). Unique catalytic properties of enzyme clusters. *Trends in Biochemical Sciences*, *3*(1), 63–65. https://doi.org/10.1016/s0968-0004(78)94045-8

Ghaemmaghami, S., Huh, W. K., Bower, K., Howson, R. W., Belle, A., Dephoure, N., O'Shea, E. K., & Weissman, J. S. (2003). Global analysis of protein expression in yeast. *Nature*, *425*(6959), 737–741. https://doi.org/10.1038/nature02046

Gipson, P., Mills, D. J., Wouts, R., Grininger, M., Vonck, J., & Kühlbrandt, W. (2010). Direct structural insight into the substrate-shuttling mechanism of yeast fatty acid synthase by electron cryomicroscopy. *Proceedings of the National Academy of Sciences*, *107*(20), 9164–9169. https://doi.org/10.1073/pnas.0913547107

Hand, S. C., & Hardewig, I. (1996). Downregulation of Cellular Metabolism During Environmental Stress: Mechanisms and Implications. *Annual Review of Physiology*, *58*(1), 539–563. https://doi.org/10.1146/annurev.ph.58.030196.002543

Hansen, J. M., Horowitz, A., Lynch, E. M., Farrell, D. P., Quispe, J., DiMaio, F., & Kollman, J. M. (2021). Cryo-EM structures of CTP synthase filaments reveal mechanism of pH-sensitive assembly during budding yeast starvation. *eLife*, *10*. https://doi.org/10.7554/elife.73368

Herrmann, J., Lerman, L. O., & Lerman, A. (2007). Ubiquitin and Ubiquitin-Like Proteins in Protein Regulation. *Circulation Research*, *100*(9), 1276–1291. https://doi.org/10.1161/01.res.0000264500.11888.f0

Heumann, J. M., Hoenger, A., Mastronarde, D. N. (2011). Clustering and variance maps for cryo-electron tomography using wedge-masked differences. *Journal of Structural Biology*, *175*(3), 288-299. https://doi.org/10.1016/j.jsb.2011.05.011

Hinzpeter, F., Tostevin, F., & Gerland, U. (2019). Regulation of reaction fluxes via enzyme sequestration and co-clustering. *Journal of The Royal Society Interface*, *16*(156), 20190444. https://doi.org/10.1098/rsif.2019.0444

Ingerson-Mahar, M., Briegel, A., Werner, J. N., Jensen, G. J., & Gitai, Z. (2010). The metabolic enzyme CTP synthase forms cytoskeletal filaments. *Nature Cell Biology*, *12*(8), 739–746. https://doi.org/10.1038/ncb2087

Jin, M., Fuller, G. G., Han, T., Yao, Y., Alessi, A. F., Freeberg, M. A., Roach, N. P., Moresco, J. J., Karnovsky, A., Baba, M., Yates, J. R., Gitler, A. D., Inoki, K., Klionsky, D. J., & Kim, J. K. (2017). Glycolytic Enzymes Coalesce in G Bodies under Hypoxic Stress. *Cell Reports*, *20*(4), 895–908. https://doi.org/10.1016/j.celrep.2017.06.082

Joyner, R. P., Tang, J. H., Helenius, J., Dultz, E., Brune, C., Holt, L. J., Huet, S., Müller, D. J., & Weis, K. (2016). A glucose-starvation response regulates the diffusion of macromolecules. *eLife*, *5*. https://doi.org/10.7554/elife.09376

Kohnhorst, C. L., Kyoung, M., Jeon, M., Schmitt, D. L., Kennedy, E. L., Ramirez, J., Bracey, S. M., Luu, B. T., Russell, S. J., & An, S. (2017). Identification of a multienzyme complex for glucose metabolism in living cells. *Journal of Biological Chemistry*, *292*(22), 9191–9203. https://doi.org/10.1074/jbc.m117.783050

Krebs, E. G., & Beavo, J. A. (1979). Phosphorylation-Dephosphorylation of Enzymes. *Annual Review of Biochemistry*, *48*(1), 923–959. https://doi.org/10.1146/annurev.bi.48.070179.004423

Kushnirov, V. V. (2000). Rapid and reliable protein extraction from yeast. *Yeast*, *16*(9), 857–860. https://doi.org/10.1002/1097-0061

Lieberman, I. (1956). Enzymatic amination of uridine triphosphate to cytidine triphosphate. *Journal of Biological Chemistry*, *222*(2), 765–775. https://doi.org/10.1016/s0021-9258(20)89934-7

Liu, J. L. (2016). The Cytoophidium and Its Kind: Filamentation and Compartmentation of Metabolic Enzymes. *Annual Review of Cell and Developmental Biology*, *32*(1), 349–372. https://doi.org/10.1146/annurev-cellbio-111315-124907

Lucas, B. A., Himes, B. A., Xue, L., Grant, T., Mahamid, J., & Grigorieff, N. (2021, June 11). Locating macromolecular assemblies in cells by 2D template matching with cisTEM. *ELife*, *10*. https://doi.org/10.7554/elife.68946

Lynch, E. M., Kollman, J. M., & Webb, B. A. (2020). Filament formation by metabolic enzymes—A new twist on regulation. *Current Opinion in Cell Biology*, *66*, 28–33. https://doi.org/10.1016/j.ceb.2020.04.006

Marini, G., Nüske, E., Leng, W., Alberti, S., & Pigino, G. (2020). Reorganization of budding yeast cytoplasm upon energy depletion. *Molecular Biology of the Cell*, *31*(12), 1232–1245. https://doi.org/10.1091/mbc.e20-02-0125

Mastronarde, D. N., & Held, S. R. (2017, February). Automated tilt series alignment and tomographic reconstruction in IMOD. *Journal of Structural Biology*, *197*(2), 102–113. https://doi.org/10.1016/j.jsb.2016.07.011

McBrien, D. C. H., & Moses, V. (1968). Compartmentation of the Metabolism of Lactose, Galactose and Glucose in Escherichia coli. *Journal of General Microbiology*, *51*(2), 159–172. https://doi.org/10.1099/00221287-51-2-159

Munder, M. C., Midtvedt, D., Franzmann, T., NüSke, E., Otto, O., Herbig, M., Ulbricht, E., Müller, P., Taubenberger, A., Maharana, S., Malinovska, L., Richter, D., Guck, J., Zaburdaev, V., & Alberti, S. (2016). A pH-driven transition of the cytoplasm from a fluid- to a solid-like state promotes entry into dormancy. *eLife*, *5*. https://doi.org/10.7554/elife.09347

Nadkarni, A. K., McDonough, V. M., Yang, W. L., Stukey, J. E., Ozier-Kalogeropoulos, O., & Carman, G. M. (1995). Differential Biochemical Regulation of the URA7- and URA8-encoded CTP Synthetases from Saccharomyces cerevisiae. *Journal of Biological Chemistry*, *270*(42), 24982–24988. https://doi.org/10.1074/jbc.270.42.24982

Noree, C., Begovich, K., Samilo, D., Broyer, R., Monfort, E., & Wilhelm, J. E. (2019). A quantitative screen for metabolic enzyme structures reveals patterns of assembly across the yeast metabolic network. *Molecular Biology of the Cell*, *30*(21), 2721–2736. https://doi.org/10.1091/mbc.e19-04-0224

Noree, C., Sato, B. K., Broyer, R. M., & Wilhelm, J. E. (2010). Identification of novel filament-forming proteins in Saccharomyces cerevisiae and Drosophila melanogaster. *Journal of Cell Biology*, *190*(4), 541–551. https://doi.org/10.1083/jcb.201003001

O'Connell, J. D., Zhao, A., Ellington, A. D., & Marcotte, E. M. (2012). Dynamic Reorganization of Metabolic Enzymes into Intracellular Bodies. *Annual Review of Cell and Developmental Biology*, *28*(1), 89–111. https://doi.org/10.1146/annurev-cellbio-101011-155841

Park, C. K., & Horton, N. C. (2019). Structures, functions, and mechanisms of filament forming enzymes: a renaissance of enzyme filamentation. *Biophysical Reviews*, *11*(6), 927–994. https://doi.org/10.1007/s12551-019-00602-6

Petrovska, I., Nüske, E., Munder, M. C., Kulasegaran, G., Malinovska, L., Kroschwald, S., Richter, D., Fahmy, K., Gibson, K., Verbavatz, J. M., & Alberti, S. (2014). Filament formation by metabolic enzymes is a specific adaptation to an advanced state of cellular starvation. *eLife*, *3*. https://doi.org/10.7554/elife.02409

Rickgauer, J. P., Grigorieff, N., & Denk, W. (2017). Single-protein detection in crowded molecular environments in cryo-EM images. *eLife*, *6*. https://doi.org/10.7554/elife.25648

Saad, S., Cereghetti, G., Feng, Y., Picotti, P., Peter, M., & Dechant, R. (2017). Reversible protein aggregation is a protective mechanism to ensure cell cycle restart after stress. *Nature Cell Biology*, *19*(10), 1202–1213. https://doi.org/10.1038/ncb3600

Saks, V., Beraud, N., & Wallimann, T. (2008). Metabolic Compartmentation – A System Level Property of Muscle Cells. *International Journal of Molecular Sciences*, *9*(5), 751–767. https://doi.org/10.3390/ijms9050751

Schmitt, D. L., & An, S. (2017). Spatial Organization of Metabolic Enzyme Complexes in Cells. *Biochemistry*, *56*(25), 3184–3196. https://doi.org/10.1021/acs.biochem.7b00249

Schindelin, J., Arganda-Carreras, I., Frise, E., Kaynig, V., Longair, M., Pietzsch, T., Preibisch, S., Rueden, C., Saalfeld, S., Schmid, B., Tinevez, J. Y., White, D. J., Hartenstein, V., Eliceiri, K., Tomancak,

P., & Cardona, A. (2012). Fiji: an open-source platform for biological-image analysis. *Nature Methods*, *9*(7), 676–682. https://doi.org/10.1038/nmeth.2019

Selivanov, V. A., Krause, S., Roca, J., & Cascante, M. (2007). Modeling of Spatial Metabolite Distributions in the Cardiac Sarcomere. *Biophysical Journal*, *92*(10), 3492–3500. https://doi.org/10.1529/biophysj.106.101352

Simonet, J. C., Burrell, A. L., Kollman, J. M., & Peterson, J. R. (2020). Freedom of assembly: metabolic enzymes come together. *Molecular Biology of the Cell*, *31*(12), 1201–1205. https://doi.org/10.1091/mbc.e18-10-0675

Suresh, H. G., da Silveira Dos Santos, A. X., Kukulski, W., Tyedmers, J., Riezman, H., Bukau, B., & Mogk, A. (2015). Prolonged starvation drives reversible sequestration of lipid biosynthetic enzymes and organelle reorganization in*Saccharomyces cerevisiae*. *Molecular Biology of the Cell*, *26*(9), 1601–1615. https://doi.org/10.1091/mbc.e14-11-1559

Sweetlove, L. J., & Fernie, A. R. (2018). The role of dynamic enzyme assemblies and substrate channelling in metabolic regulation. *Nature Communications*, *9*(1). https://doi.org/10.1038/s41467-018-04543-8

Tange, O. (2011). GNU parallel – the command-line power tool. USENIX Magazine, *36*(1), 42–47.

Wang, Q., Zhang, Y., Yang, C., Xiong, H., Lin, Y., Yao, J., Li, H., Xie, L., Zhao, W., Yao, Y., Ning, Z. B., Zeng, R., Xiong, Y., Guan, K. L., Zhao, S., & Zhao, G. P. (2010). Acetylation of Metabolic Enzymes Coordinates Carbon Source Utilization and Metabolic Flux. *Science*, *327*(5968), 1004–1007. https://doi.org/10.1126/science.1179687

Weigert, M., Schmidt, U., Boothe, T., Müller, A., Dibrov, A., Jain, A., Wilhelm, B., Schmidt, D., Broaddus, C., Culley, S., Rocha-Martins, M., Segovia-Miranda, F., Norden, C., Henriques, R., Zerial, M., Solimena, M., Rink, J., Tomancak, P., Royer, L., . . . Myers, E. W. (2018). Content-aware image restoration: pushing the limits of fluorescence microscopy. *Nature Methods*, *15*(12), 1090–1097. https://doi.org/10.1038/s41592-018-0216-7

Yang, W. L., McDonough, V. M., Ozier-Kalogeropoulos, O., Adeline, M. T., Flocco, M. T., & Carman, G. M. (1994). Purification and Characterization of CTP Synthetase, the Product of the URA7 Gene in Saccharomyces cerevisiae. *Biochemistry*, *33*(35), 10785–10793. https://doi.org/10.1021/bi00201a028

Zhou, X., Guo, C. J., Chang, C. C., Zhong, J., Hu, H. H., Lu, G. M., & Liu, J. L. (2021). Structural basis for ligand binding modes of CTP synthase. *Proceedings of the National Academy of Sciences*, *118*(30). https://doi.org/10.1073/pnas.2026621118